IJEAS

# International Journal of Engineering & Applied Sciences

IJEAS

# Editorial Board

# Abstracting & Indexing

IJEAS provides unique DOI link to every paper published.

# Editorial Scope

The journal presents its readers with broad coverage across some branches of engineering and science of the latest development and application of new solution algorithms, artificial intelligent techniques innovative numerical methods and/or solution techniques directed at the utilization of computational methods in solid and nano-scaled mechanics.

International Journal of Engineering & Applied Sciences (IJEAS) is an Open Access Journal

International Journal of Engineering & Applied Sciences (IJEAS) publish original contributions on the following topics:

Numerical Methods in Solid Mechanics

Nanomechanic and applications

Microelectromechanical systems (MEMS)

Vibration Problems in Engineering

Higher order elasticity (Strain gradient, couple stress, surface elasticity, nonlocal elasticity) Applied Mathematics

IJEAS allows readers to read, download, copy, distribute, print, search, or link to the full texts of articles.

# CONTENTS

# Elastic Stresses of Rotating Transversely Isotropic Fiber Reinforced Composite Cylinders

*Ömer Can Farukoğlu* [a*]*, İhsan Korkut* [b]

[a,b] *Department of Manufacturing Engineering, Gazi University, Ankara, Turkey.*
*E-mail address*: omerfarukoglu08@gmail.com [a], ikorkut@gazi.edu.tr [b]

*ORCID numbers of author:*
*0000-0003-3244-8355*[a]*, 0000-0002-5001-4449*[b]

## Abstract

*In this study, rotating long thick-walled fiber reinforced composite cylinders with closed ends are investigated within the elastic limits by using analytical methods. Hoffman yield criterion is employed to the elastic problem to find limit angular velocities. Composite bodies of the cylinders are consisting of isotropic matrix and transversely isotropic fibers which are unidirectionally aligned in the circumferential direction. Alterations on the elastic stress and displacement fields are examined by taking various fiber volume fraction and wall thickness values. Obtained results emphasize that both parameters highly influence the distributions of stress, displacement, and commencement of the yielding.*

**Keywords:** Rotating cylinders; composite cylinders; stress analysis; analytical methods

## 1. Introduction

In many engineering applications, cylindrical components such as disks, cylinders, and rods are often utilized. Hence, it is highly crucial to forecast stress and displacement distributions in such geometries. According to the developments in material science and the needs in engineering, axisymmetric components have started to be produced from different materials. Fiber reinforced composites have become exceedingly popular among scientists and engineers due to the advantageous material properties. In this regard, stress analyses of axisymmetric components, which are made of different materials, under various loading conditions can be found extensively in the literature. Stress analyses of rotating functionally graded material (fgm) disks have been broadly examined by the use of analytical and numerical methods [1-5]. Deformations and stresses of pressurized fgm cylinders and tubes can be found in the publications as well [6-10]. Similar studies are also carried out for orthotropic cylindrical structures. Rotating orthotropic disks have been the subject of various engineering studies [11-14]. Likewise, solutions have been proposed to orthotropic cylinder investigations with [15,16] or without [17,18] the influence of thermal stresses. Several studies focus on composite disks as well. Stress and displacement fields of solid, annular, and variable thickness rotating fiber reinforced disks are available [19-21]. On the other hand, the number of researches for the fiber reinforced disks and cylinders is lower than the same geometries made of functionally graded

or orthotropic materials. Thus, this study is aiming to give more insight into fiber reinforced cylinders by employing analytical methods.

In this research, rotating long thick-walled composite cylinders with fixed ends are studied in the framework of elasticity. The composite material of the cylinders consisting of isotropic matrix and transversely isotropic fibers. The alignment of the fibers is taken unidirectionally through the circumferential direction. Thus, the circumferential direction becomes the longitudinal ($L$) direction, and the remaining radial and axial directions of the cylinders turn out to be the transverse ($T$) directions. In Fig. 1 (a), these directions and the composite cylinders are visualized. In Fig. 1 (b), fiber reinforced composite material is demonstrated with the material coordinate system. Correspondingly, lower case $l$ and $t$ point to the longitudinal (fiber) and transverse directions of the composite material, where $m$ and $f$ denote matrix and fibers as well. In the elastic limit calculations, Hoffman yield criterion [22] is exploited to obtain elastic limit angular velocity and commencement of the yielding through the thickness of the cylinders.
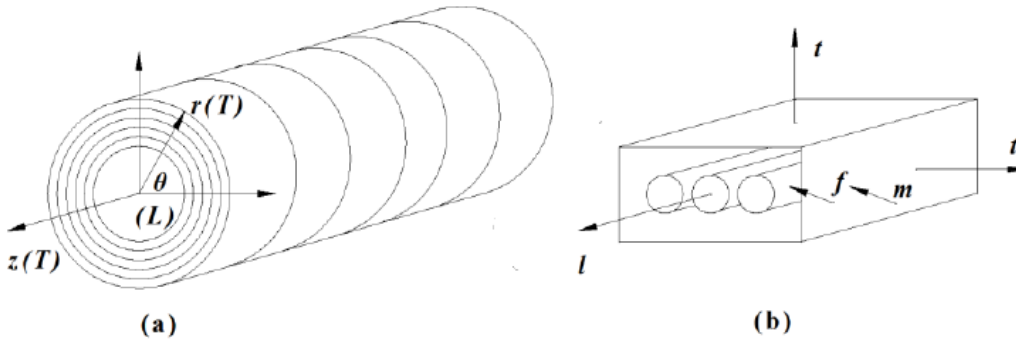


Fig.1. (a) Rotating cylinders with central hole, (b) Composite material

## 2. Mechanical Property Calculations

Several models can be supplied from the literature to calculate the mechanical properties of the fiber reinforced composites. In the present work, Chamis method [23,24] is utilized due to its usefulness and simple implementation. $V_m$ and $V_f$ denote the volume fraction of the matrix and fibers in Eq.(1).

$$V_m = 1 - V_f \tag{1}$$

Elastic modulus of the composite material in the longitudinal ($E_L$) and transverse ($E_T$) directions are calculated via Eqs.(2)-(3)

$$E_L = V_f E_{lf} + V_m E_m \tag{2}$$

$$E_T = \frac{E_m}{1 - \sqrt{V_f}\left(1 - \frac{E_m}{E_{tf}}\right)} \tag{3}$$

where $E_{lf}$ and $E_{tf}$ express elastic modulus of the transversely isotropic fibers in the longitudinal and transverse directions. $E_m$ is the elastic modulus of the matrix. Followingly, Poisson's ratios of the composite material in different directions ($v_{LT}$, $v_{TL}$, $v_{TT}$) are presented

$$v_{LT} = V_f v_{ltf} + V_m v_m \tag{4}$$

$$v_{TL} = v_{LT} \frac{E_T}{E_L} \tag{5}$$

$$v_{TT} = V_f v_{ttf} + V_m(2v_m - v_{TL}) \tag{6}$$

in which $v_{ltf}$ and $v_{ttf}$ are the Poisson's ratios of the fibers in *l-t* and *t-t* directions. Poisson's ratio of the isotropic matrix is indicated with $v_m$. In the following equation, density of the composite ($\rho$) is calculated where $\rho_f$ and $\rho_m$ signify density of the fibers and matrix

$$\rho = V_f \rho_f + V_m \rho_m \tag{7}$$

According to the fiber failure mode, such as micro buckling or fracture due to shear, there are many different models to estimate the elastic limits of the composite materials in different directions. In this study, the models proposed by Chamis to estimate the tensile and compressive strength of the composite are used for convenience. In this regard, the longitudinal tensile ($L_T$) and compressive ($L_c$) strength of the composite are calculated by Eq.(8) and Eq.(9)

$$L_T = V_f L_{tf} \tag{8}$$

$$L_c = V_f L_{cf} \tag{9}$$

in which $L_{tf}$ and $L_{cf}$ are the longitudinal tensile and compressive strength of the fibers. Transverse tensile ($T_T$) and compressive ($T_C$) strengths are as follows

$$T_T = T_{tm}[1 - (\sqrt{V_f} - V_f)(1 - \frac{E_m}{E_{tf}})] \tag{10}$$

$$T_C = T_{cm}[1 - (\sqrt{V_f} - V_f)(1 - \frac{E_m}{E_{tf}})] \tag{11}$$

in Eqs.(10)-(11), terms that are titled as $T_{tm}$ and $T_{cm}$ express tensile and compressive strengths of the matrix material.


## 3. Analytical Solution

In order to define elastic relations, cylindrical polar coordinate system ($r, \theta, z$) is exploited. Radial, tangential, and axial elastic strains are given below

$$\varepsilon_r = \frac{du_r(r)}{dr}, \varepsilon_\theta = \frac{u_r(r)}{r}, \varepsilon_z = 0 \tag{12}$$

where $u_r(r)$ is the radial displacement. Due to the axial symmetry of the cylinders, displacement is function of $r$ only. In addition, the axial strain is equal to zero since the ends of the cylinders are considered as fixed. As can be noticed, strain-displacement relation is defined at Eq.(12), and the composite material properties are calculated in the above section. Under these conditions, strain-stress relation can be determined adequately. Recalling from the definition of the problem that the fibers are unidirectionally aligned in the circumferential direction, and the remaining radial and axial directions of the cylinders are taken as transverse. These considerations yield to the following compliance matrix, which portrays the strain-stress relation

$$\begin{bmatrix} \varepsilon_r \\ \varepsilon_\theta \\ \varepsilon_z \end{bmatrix} = \begin{bmatrix} \dfrac{1}{E_T} & -\dfrac{v_{LT}}{E_L} & -\dfrac{v_{TT}}{E_T} \\ -\dfrac{v_{TL}}{E_T} & \dfrac{1}{E_L} & -\dfrac{v_{TL}}{E_T} \\ -\dfrac{v_{TT}}{E_T} & -\dfrac{v_{LT}}{E_L} & \dfrac{1}{E_T} \end{bmatrix} \begin{bmatrix} \sigma_r \\ \sigma_\theta \\ \sigma_z \end{bmatrix} \tag{13}$$

in which $\sigma_r$, $\sigma_\theta$ and $\sigma_z$ express radial, tangential, and axial stresses respectively. Correspondingly, elastic stress-strain relation is obtained with the indicated below stiffness matrix

$$\begin{bmatrix} \sigma_r \\ \sigma_\theta \\ \sigma_z \end{bmatrix} = \begin{bmatrix} \dfrac{1 - v_{LT}v_{TL}}{E_L E_T \Delta} & \dfrac{v_{LT}(1 + v_{TT})}{E_L E_T \Delta} & \dfrac{v_{TT} + v_{LT}v_{TL}}{E_L E_T \Delta} \\ \dfrac{v_{TL}(1 + v_{TT})}{E_T{}^2 \Delta} & \dfrac{1 - v_{TT}{}^2}{E_T{}^2 \Delta} & \dfrac{v_{TL}(1 + v_{TT})}{E_T{}^2 \Delta} \\ \dfrac{v_{TT} + v_{LT}v_{TL}}{E_L E_T \Delta} & \dfrac{v_{TL}(1 + v_{TT})}{E_L E_T \Delta} & \dfrac{1 - v_{LT}v_{TL}}{E_L E_T \Delta} \end{bmatrix} \begin{bmatrix} \varepsilon_r \\ \varepsilon_\theta \\ \varepsilon_z \end{bmatrix}, \tag{14}$$

$$\Delta = \frac{(1 + v_{TT})(1 - v_{TT} - 2v_{AT}v_{TA})}{E_A E_T{}^2}$$

It is to be remarked that both compliance and stiffness matrices are symmetrical and obey Hook's law. In the following, the compatibility condition for the elastic problem is given

$$r \frac{d\varepsilon_\theta}{dr} + \varepsilon_\theta - \varepsilon_r = 0 \tag{15}$$

The compatibility condition is fulfilled by substituting radial and tangential strains given in Eq.(12) to the above equation. The non-trivial equilibrium equation for this problem is of the form

$$\frac{d\sigma_r}{dr} + \frac{1}{r}(\sigma_r - \sigma_\theta) + \rho\omega^2 r = 0 \tag{16}$$

where $\omega$ is the angular velocity. To be able to solve Eq.(16), initially, directional strain terms presented in Eq.(12) should be substituted into Eq.(14). Followingly, elastic stresses in Eq.(14) are substituted to Eq.(16). After several algebraic procedures, a non-homogeneous Cauchy Euler type differential equation is obtained

$$r^2 \frac{du_r^2}{dr^2} + r \frac{u_r}{dr} - \frac{s_{22}}{s_{11}} u_r = -\frac{\rho\omega^2}{s_{11}} r^3 \tag{17}$$

$s_{ij}$ $(i,j = 1,2,3)$ terms used above are the terms of the stiffness matrix given in Eq.(14). In order to solve the homogeneous part of the above differential equation, in other words, the left-hand side of Eq.(17), we may propose a solution as $u_r = r^\lambda$ in which $\lambda$ is an unknown constant. Successively, $u_r' = \lambda r^{\lambda-1}$ and $u_r'' = \lambda(\lambda - 1)r^{\lambda-2}$ where the superscript (') denotes the derivative. By substituting $u_r$, $u_r'$ and $u_r''$ into Eq.(17) and setting the right-hand side of the equation as zero, we obtain the homogeneous solution of Eq.(17) which is named $u_h(r)$

$$u_h(r) = C_1 r^{-\alpha_1} + C_2 r^{\alpha_1}, \text{ and } \alpha_1 = \sqrt{\frac{s_{22}}{s_{11}}} = \sqrt{\frac{E_L(1-v_{TT}^2)}{E_T(1-v_{LT}v_{TL})}} \tag{18}$$

In the above equation, $C_1$ and $C_2$ are the arbitrary constants. The next step is finding the particular solution ($u_P(r)$) of Eq.(17). The method of variation of parameters is employed for this purpose.

$$u_P(r) = Q_1(r)u_1(r) + Q_2(r)u_2(r) \tag{19}$$

$u_1$ and $u_2$ are the two homogeneous solutions of Eq.(17) which are equal to $r^{-\alpha_1}$ and $r^{\alpha_1}$ respectively

$$Q_1(r) = -\int \frac{P(r)u_2}{u_1 u_2' - u_1' u_2} dr, \qquad Q_2(r) = \int \frac{P(r)u_1}{u_1 u_2' - u_1' u_2} dr \tag{20}$$

in which $P(r) = -(\rho\omega^2/s_{11})r$. $P(r)$ is simply found by dividing Eq.(17) with $r^2$ and taking the right-hand side of the remaining equation. To be able to utilize the method of variation of parameters, the coefficient of the highest order derivative must be 1. The particular solution of Eq.(17) takes the below form after these mathematical operations

$$u_P(r) = \alpha_2 r^3, \alpha_2 = \frac{\rho\omega^2}{s_{22}-9s_{11}} = \frac{\Delta E_L E_T^2 \rho\omega^2}{E_L(1-v_{TT}^2)-9E_T(1-v_{LT}v_{TL})} \tag{21}$$

Finally, radial displacements of the composite cylinders are achieved by adding the homogeneous and particular solutions stated in Eq.(18) and Eq.(21)

$$u_r(r) = C_1 r^{-\alpha_1} + C_2 r^{\alpha_1} + \alpha_2 r^3 \tag{22}$$

Directional elastic strains can be written of the form by applying Eq.(12) to the above equation

$$\varepsilon_r(r) = -C_1\alpha_1 r^{-\alpha_1-1} + C_2\alpha_1 r^{\alpha_1-1} + 3\alpha_2 r^2 \tag{23}$$

$$\varepsilon_\theta(r) = C_1 r^{-\alpha_1-1} + C_2 r^{\alpha_1-1} + \alpha_2 r^2 \tag{24}$$

It should be reminded that due to the fixed ends of the geometry, the axial strain is equal to zero. Subsequently, if Eq.(23) and Eq.(24) are implemented to Eq.(14), directional elastic stresses become

$$\sigma_r(r) = -C_1 r^{-\alpha_1-1}(\alpha_1 s_{11} - s_{12}) + C_2 r^{\alpha_1-1}(\alpha_1 s_{11} + s_{12}) + \alpha_2 r^2(3s_{11} + s_{12}) \tag{25}$$

$$\sigma_\theta(r) = -C_1 r^{-\alpha_1-1}(\alpha_1 s_{21} - s_{22}) + C_2 r^{\alpha_1-1}(\alpha_1 s_{21} + s_{22}) + \alpha_2 r^2(3s_{21} + s_{22}) \tag{26}$$

$$\sigma_z(r) = -C_1 r^{-\alpha_1-1}(\alpha_1 s_{31} - s_{32}) + C_2 r^{\alpha_1-1}(\alpha_1 s_{31} + s_{32}) + \alpha_2 r^2(3s_{31} + s_{32}) \tag{27}$$

in which $s_{ij}$ terms, once again, express the components of the stiffness matrix in Eq.(14). In the case of rotating cylinders with central holes, $C_1$ and $C_2$ are found by the following boundary conditions

$$\sigma_r(a) = 0, \qquad \sigma_r(b) = 0 \tag{28}$$

in which $a$ and $b$ present inner and outer radii of the cylinders. If the boundary conditions are exerted to Eq.(25), arbitrary constants can be carried out

$$C_1 = \frac{\alpha_2(a^{2\alpha_1}b^{3+\alpha_1} - a^{3+\alpha_1}b^{2\alpha_1})(3s_{11} + s_{12})}{(a^{2\alpha_1} - b^{2\alpha_1})(\alpha_1 s_{11} - s_{12})} \tag{29}$$

$$C_2 = -\frac{\alpha_2(a^{3+\alpha_1} - b^{3+\alpha_1})(3s_{11} + s_{12})}{(a^{2\alpha_1} - b^{2\alpha_1})(\alpha_1 s_{11} + s_{12})} \tag{30}$$

As previously stated, Hoffman yield criterion is employed to calculate the elastic limits of the cylinders. The general form of the corresponding criterion in principal directions is

$$\begin{aligned}
&\frac{1}{2}\left(-\frac{1}{X_T X_C} + \frac{1}{Y_T Y_C} + \frac{1}{Z_T Z_C}\right)(\sigma_\theta - \sigma_z)^2 + \frac{1}{2}\left(\frac{1}{X_T X_C} - \frac{1}{Y_T Y_C} + \frac{1}{Z_T Z_C}\right)(\sigma_z - \sigma_r)^2 + \\
&\frac{1}{2}\left(\frac{1}{X_T X_C} + \frac{1}{Y_T Y_C} - \frac{1}{Z_T Z_C}\right)(\sigma_r - \sigma_\theta)^2 + \left(\frac{1}{X_T} - \frac{1}{X_C}\right)\sigma_r + \left(\frac{1}{Y_T} - \frac{1}{Y_C}\right)\sigma_\theta + \\
&\left(\frac{1}{Z_T} - \frac{1}{Z_C}\right)\sigma_z \leq 1
\end{aligned} \tag{31}$$

at Eq.(31), *X, Y, Z* express the yield strength of the material at the corresponding direction, and the subscripts *T* and *C* clarify either the load is tensile or compressive. In-between equations Eqs.(8)-(11), composite material strengths have previously been introduced. By operating Eq.(8) to Eq.(11) with Eq.(31), Hoffman yield criteria can be adapted to this case

$$\begin{aligned}
\sigma_Y(r) = &\frac{1}{2L_T L_C}[(\sigma_\theta - \sigma_z)^2 + (\sigma_r - \sigma_\theta)^2] + \frac{1}{2}\left(\frac{2}{T_T T_C} - \frac{1}{L_T L_C}\right)(\sigma_z - \sigma_r)^2 \\
&+ \left(\frac{1}{T_T} - \frac{1}{T_C}\right)(\sigma_r + \sigma_z) + \left(\frac{1}{L_T} - \frac{1}{L_C}\right)\sigma_\theta \leq 1
\end{aligned} \tag{32}$$

Eq.(32) is the corresponding yield criteria, which is named $\sigma_Y(r)$ and is going to be used to find the elastic limit angular velocity of the cylinders. If the value of the obtained $\omega$ is exceeded, then the elastic region gets exited. In other words, from Eq.(12) to this point, all elastic equations are valid as long as $\sigma_Y(r) \leq 1$. Thus, limit angular velocity values are obtained when $\sigma_Y(r) = 1$.

## 3. Numerical Examples

After analytical modeling, to exemplify numerical results, dimensions of the composite cylinders and the properties of the cylinder material are assigned. In this regard, to understand how the wall thickness of the cylinders changes the distribution of the elastic stresses, outer radii ($b$) of the cylinders are kept constant as 0.1 m, and various inner radii ($a$) values (0.02 m, 0.05 m, 0.08 m) are taken. So that the inner/outer radius ratio ($a/b$) becomes 0.2, 0.5 and 0.8 respectively. As the fiber reinforced composite, graphite/epoxy is used. Properties of the epoxy and transversely isotropic graphite fibers are tabulated below

Table 1. Mechanical Properties of the Epoxy and Graphite Fibers [25]

| $E_{lf}$ | $E_{tf}$ | $E_m$ | $\nu_{ltf}$ | $\nu_{ttf}$ | $\nu_m$ | $\rho_f$ | $\rho_m$ | $L_{tf}$ | $L_{cf}$ | $T_{tm}$ | $T_{cm}$ |
|---|---|---|---|---|---|---|---|---|---|---|---|
| $(GPa)$ | $(GPa)$ | $(GPa)$ | $(-)$ | $(-)$ | $(-)$ | $(\frac{kg}{m^3})$ | $(\frac{kg}{m^3})$ | $(MPa)$ | $(MPa)$ | $(MPa)$ | $(MPa)$ |
| 230 | 22 | 3.4 | 0.30 | 0.35 | 0.30 | 1800 | 1200 | 2067 | 1999 | 72 | 102 |

Material properties are obtained for three different fiber volume fraction values ($V_f = 0.20$, 0.50, 0.80) via operating Chamis method, which is given from (1) to (11), with the properties in Table 1. Accordingly, one can investigate the influences of $V_f$ on the elastic stress and displacement fields. At this stage, variables are transformed to their normalized forms which are expressed with overbars. Hence, radial coordinate is $\bar{r} = r/b$. Directional stresses take the following forms $\bar{\sigma}_j(r) = \sigma_j(r)/\sigma_o$ where $j = r, \theta, z$ and the yield stress is $\bar{\sigma}_Y(r) = \sigma_Y(r)$. Normalized angular velocity can be written as $\bar{\omega} = \omega b \sqrt{\rho_o/\sigma_o}$. Non-dimensional radial displacement is transformed to $\bar{u}_r(r) = u_r(r)E_o/\sigma_o b$. Lastly, arbitrary constant are of the following $\bar{C}_1 = C_1/b^{1+\alpha_1}$ and $\bar{C}_2 = C_2/b^{1-\alpha_1}$. In the normalization procedure $\sigma_o$, $E_o$ and $\rho_o$ are introduced. These constants are as follows

$$\sigma_o = \frac{1}{4}\sqrt{\left(\frac{L_{tf}+L_{cf}+T_{tm}+T_{cm}}{4}\right)^2}, \quad E_o = \frac{1}{3}\sqrt{\left(\frac{E_{lf}+E_{tf}+E_m}{3}\right)^2} \text{ and } \rho_o = \frac{\rho_f+\rho_m}{2} \tag{33}$$

After the boundary conditions stated in Eq.(29) and Eq.(30) are employed to stresses and displacements, elastic limit angular velocity and the beginning of the yielding are calculated by the use of Eq.(32). The results obtained for various $a/b$ and $V_f$ are exhibited in Table 2. It is to be noted that the position of the yielding is denoted with $\bar{r}_Y$ in Table 2

Table 2. Calculated dimensionless arbitrary constants, elastic limit angular velocities and position of the yielding for various $V_f$ and $a/b$

|  |  | $V_f = 0.20$ | $V_f = 0.50$ | $V_f = 0.80$ |
|---|---|---|---|---|
| $a/b = 0.2$ | $\bar{C}_1$ | $6.67953 \times 10^{-6}$ | $7.69944 \times 10^{-7}$ | $4.93349 \times 10^{-7}$ |
|  | $\bar{C}_2$ | 0.0341764 | -0.0388193 | -0.0243708 |
|  | $\bar{r}_Y$ | 0.618322 | 0.645025 | 0.634944 |
|  | $\bar{\omega}$ | 1.56408 | 1.8232 | 1.84966 |
| $a/b = 0.5$ | $\bar{C}_1$ | 0.000354862 | 0.000141208 | 0.000103404 |
|  | $\bar{C}_2$ | 0.0316035 | -0.0445137 | -0.0298333 |
|  | $\bar{r}_Y$ | 0.5 | 0.720314 | 0.722186 |
|  | $\bar{\omega}$ | 1.49828 | 1.95469 | 2.04922 |
| $a/b = 0.8$ | $\bar{C}_1$ | 0.001605 | 0.00120456 | 0.00109806 |
|  | $\bar{C}_2$ | 0.0263474 | -0.0435268 | -0.0351421 |
|  | $\bar{r}_Y$ | 0.8 | 0.8 | 0.8 |
|  | $\bar{\omega}$ | 1.34404 | 1.95086 | 2.24789 |

It is depicted in the results in Table 2 that elastic limit angular velocity increases with higher fiber volume fraction. In other words, when the fiber volume fraction elevates, cylinders begin yielding at higher strengths. Whereas, it is hard to make a clear statement for the influence of the $a/b$ ratio. When $V_f$=0.20 and $a/b$ ratio is increasing from 0.20 to 0.80, calculated elastic limit angular velocities decreas. On the other hand, when $V_f$=0.80 and $a/b$ ratio rises, composite cylinders tend to fail at higher $\bar{\omega}$. Thus, one can conclude that the wall thickness of the composite cylinders should be treated carefully to get optimum results. In order to understand this phenomenon, Figure 2 is illustrated below. According to the plotting, when fiber volume fraction in the composite is low ($V_f$=0.20), thick-walled cylinders ($a/b$=0.20) are prone to yield at greater $\bar{\omega}$. However, as $V_f$ increases in the composite, cylinders that have thinner wall-thickness ($a/b$=0.80) start plastic flow at higher $\bar{\omega}$.
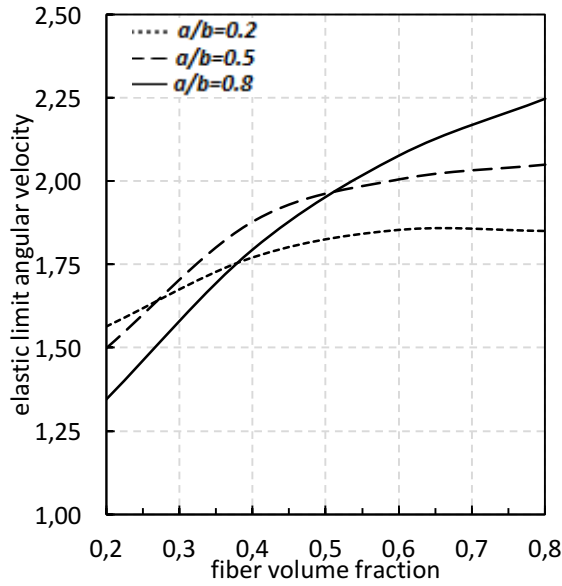
Fig. 2. Distribution of the elastic limit angular velocity for the cylinders having different $a/b$ and $V_f$

In the following figures, corresponding elastic stress and displacement fields are presented. As can be noticed in Figure 3 (a), (b), and (c), when $a/b$=0.2, plastic flow commences in the middle of the cylinders. On the other hand, as the thickness of the cylinder walls gets slender, yielding begins at the inner radii. For instance, all cylinders begin yielding at $r = a$ when $a/b$=0.8. The position of the yielding ($\bar{r}_Y$) is calculated when $\bar{\sigma}_Y(r)$=1, and the exact position of $\bar{r}_Y$ is given in Table 2
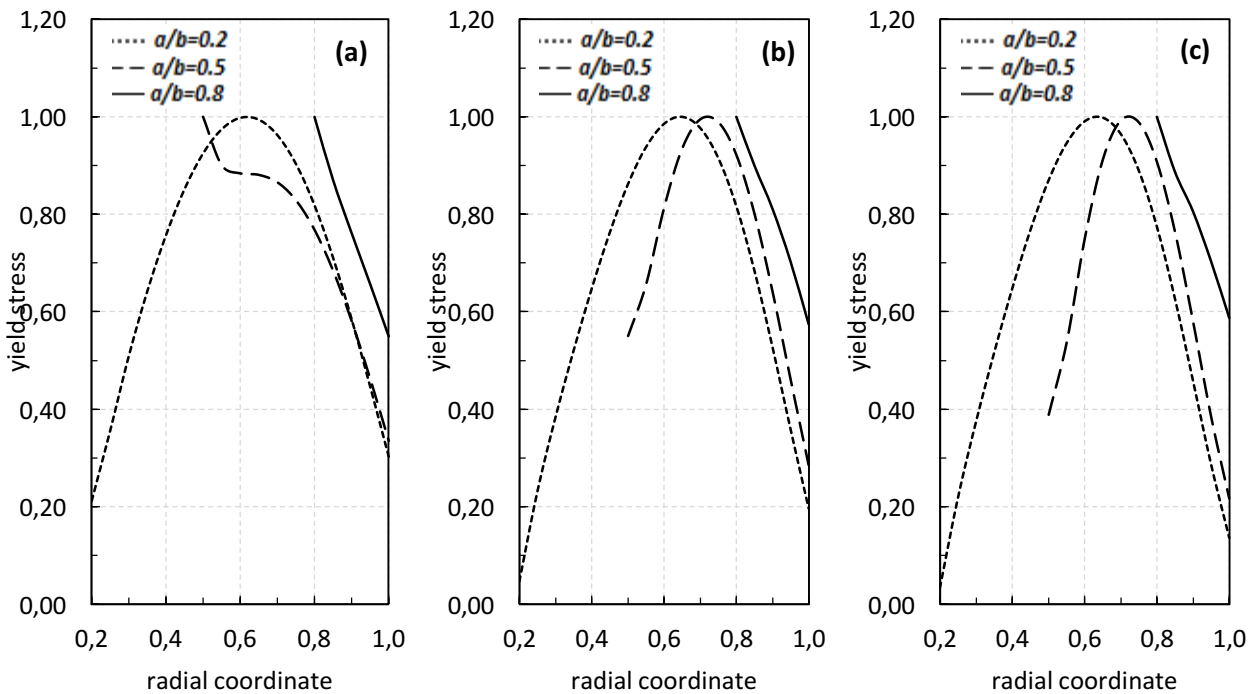


Fig. 3. Variation of the dimensionless yield stress along $\bar{r}$ for various $a/b$ ratios where (a) $V_f$=0.20, (b) $V_f$=0.50 and (c) $V_f$=0.80

In the subsequent set of figures, non-dimensional elastic limit radial stresses are presented. It is observed from Figure 4 (a), (b), and (c) that radial stresses increase as $V_f$ enlarges for the cylinders with the same $a/b$ ratio. The graphs below also reveal that the cylinders with higher wall thicknesses ($a/b$=0.2) have higher radial stress compared to the lower ones ($a/b$=0.8). In the ensuing plotting, tangential stresses are exhibited
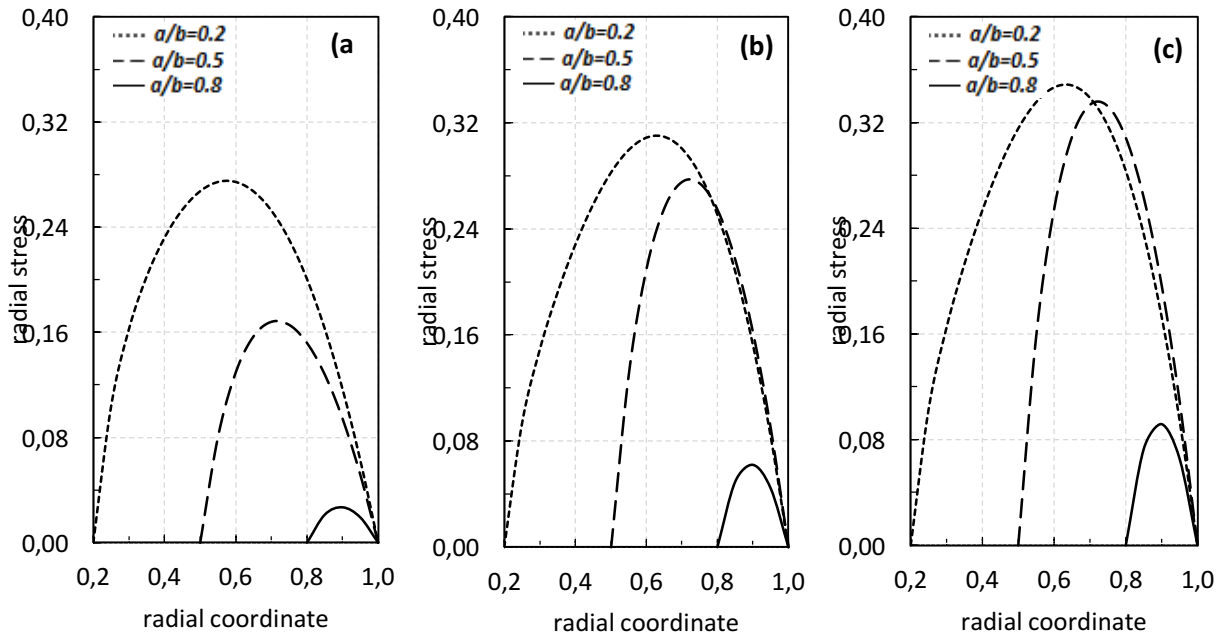


Fig. 4. Variation of the dimensionless radial stress along $\bar{r}$ for various $a/b$ ratios where (a) $V_f$=0.20, (b) $V_f$=0.50 and (c) $V_f$=0.80
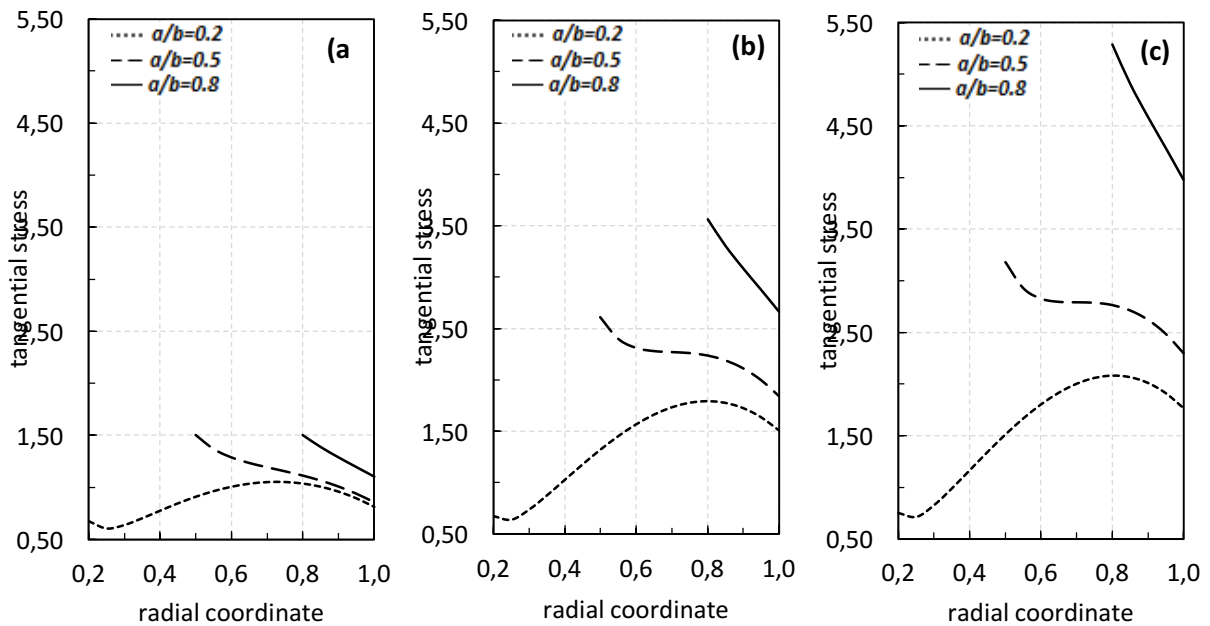


Fig. 5. Variation of the dimensionless tangential stress along $\bar{r}$ for various $a/b$ ratios where (a) $V_f$=0.20, (b) $V_f$=0.50 and (c) $V_f$=0.80

According to Figure 5 (a), (b), and (c), normalized tangential stresses enlarge, when $V_f$ amplifies for cylinders with the same $a/b$ ratio. On the other hand, while the radial stresses are high in the thick-walled cylinders ($a/b$=0.2), tangential stress components are high in the thinner ones ($a/b$=0.8). Another important issue is that the magnitudes of the elastic limit tangential stresses are significantly higher than the radial stresses. In the next figure, axial stresses are presented in Figure 6 (a), (b), and (c). Fiber volume fraction slightly influences the axial stresses when $a/b$=0.2. Conversely, as the wall thickness gets smaller, the effect of $V_f$ becomes more apparent and the profiles of the axial stress components tend to skew to the outer radii of the cylinders.
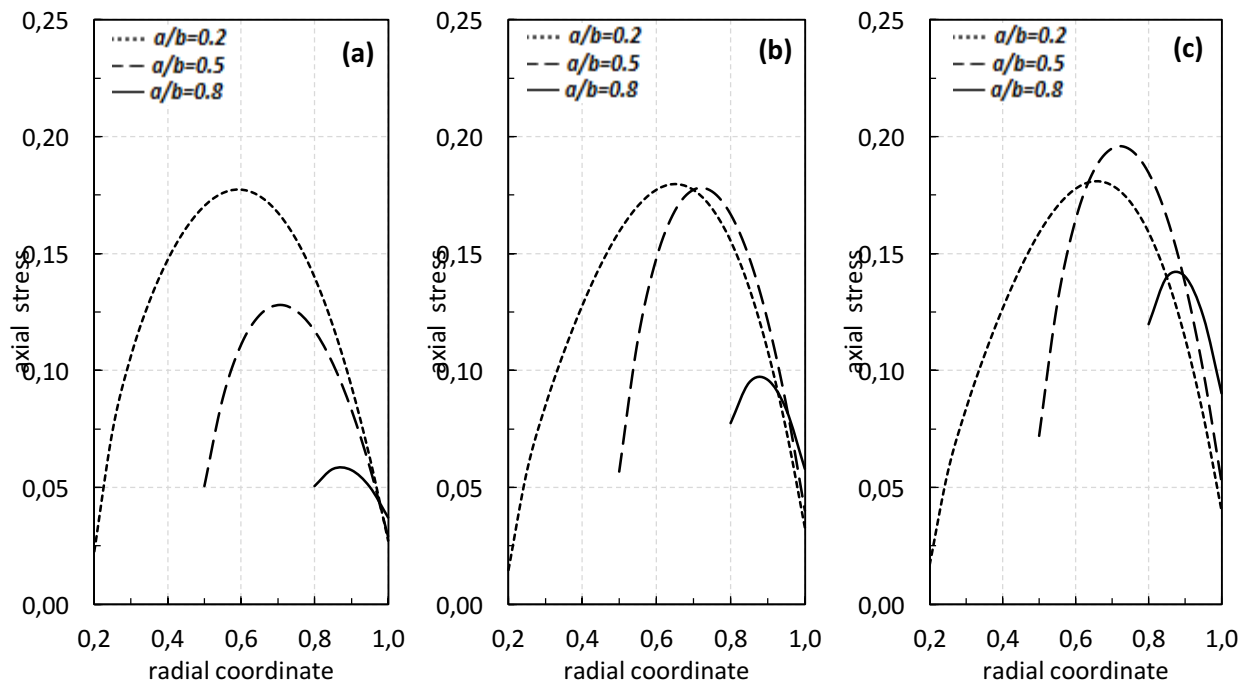


Fig. 6. Variation of the dimensionless axial stress along $\bar{r}$ for various $a/b$ ratios where (a) $V_f$=0.20, (b) $V_f$=0.50 and (c) $V_f$=0.80

In the final figure demonstrated below, normalized radial displacements are portrayed. In accordance with Figure 7 (a), (b), and (c), radial displacements of the cylinders sharing the same $a/b$ reduce as $V_f$ goes up. For the cylinders having the same $V_f$, radial displacements are highly affected by $a/b$. When the cylinders are having narrower walls, the magnitudes of the radial displacements are at high levels. However, the radial displacement differences of the inner and outer radii of the cylinders become greater in the thick-walled ones. Another remark that should be noted is that the distribution profiles of the radial displacements and tangential stresses are markedly analogous. The resemblance can be noticed by comparing Figures 5 and 7.
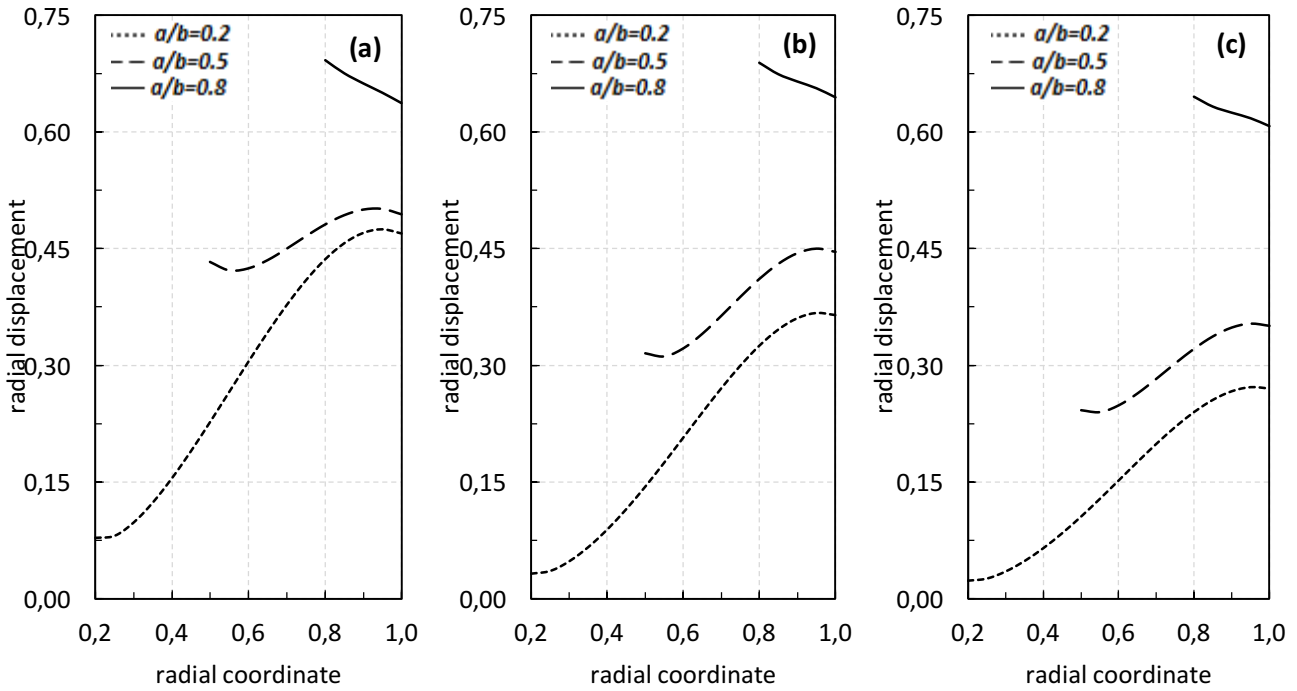
Fig. 7. Variation of the dimensionless radial displacement along $\bar{r}$ for various $a/b$ ratios where (a) $V_f$=0.20, (b) $V_f$=0.50 and (c) $V_f$=0.80

## 5. Conclusion

In this study, the rotating fiber reinforced composite cylinders subjected to free-free boundary conditions are studied by employing analytical methods. The elastic stress and displacement fields are investigated for numerous wall thickness ($a/b$) and fiber volume ($V_f$) ratios. It has been seen that these fields are immensely altered by $a/b$ and $V_f$. Hoffman yield criterion is adapted to the problem and elastic limits are obtained accordingly. One can conclude from the calculated results that as $V_f$ in the composite increases, yielding initiates at higher angular velocities. Whereas, $a/b$ ratio should be utilized cautiously. If the wall thickness ratio is not selected properly, yielding in the cylinders may occur at lower angular velocities. The commencement of the plastic flow varies according to the assigned $a/b$ and $V_f$. When the cylinder walls are thick, yielding tends to begin in the middle of the cylinder walls. However, as the wall thickness becomes smaller, yielding starts at the inner radii of the cylinders. Also, according to the elastic limit stress and displacement fields that we get, magnitudes of radial and axial stresses are considerably small when compared to tangential ones, and as the cylinder walls get thinner tangential stress components majorly rise.

## References

[1] Dai, T., Dai, H. L., Investigation of mechanical behavior for a rotating fgm circular disk with a variable angular speed, *Journal of Mechanical Science and Technology*, 29(9), 3779-3787, 2015.

[2] Eraslan, A. N., Arslan, E., Analytical and numerical solutions to rotating fgm disk, *Journal of Multidisciplinary Engineering Science and Technology*, 2(10), 2843-2850, 2015.

[3] Zheng, Y., Bahaloo, H., Mousanezhad, D., Mahdi, E., Vaziri, A., Nayeb-Hashemi, H., Stress analysis in functionally graded rotating disks with non-uniform thickness and variable angular velocity, *International Journal of Mechanical Sciences*, 119, 283-293, 2016.

[4] Çallıoğlu, H., Bektaş, N. B., Sayer, M., Stress analysis of functionally graded rotating disc: analytical and numerical solutions, *Acta Mechanica Sinica*, 27(6), 950-955, 2011.

[5] Horgan, C. O., Chan, A. M., The stress response of functionally graded isotropic linearly elastic rotating disks, *Journal of Elasticity*, 55(3), 219-230, 1999.

[6] Yıldırım, V., Effects of inhomogeneity and thickness parameters on the elastic response of a pressurized hyperbolic annulus/disc made of functionally graded material, *International Journal of Engineering & Applied Sciences (IJEAS)*, 9(3), 36-50, 2017.

[7] Dui, G., Zhou, D., Solutions for behavior of a functionally graded thick-walled tube subjected to mechanical and thermal loads, *International Journal of Mechanical Sciences*, 98, 70-79, 2015.

[8] Dui, G., Zhang, J., An elasticity solution for functionally graded thick-walled tube subjected to internal pressure, *International Journal of Mechanical Sciences*, 89, 344-349, 2014.

[9] Tütütncü, N., Stresses in thick-walled FGM cylinders with exponentially-varying properties, *Engineering Structures*, 29(9), 2032-2035, 2007.

[10] Nejad, M. Z., Rahimi, G. H., Deformations and stresses in rotating fgm pressurized thick hollow cylinder under thermal load, *Scientific Research and Essays*, 4(3), 131-140, 2009.

[11] Nie, G. J., Zhong, Z., Batra, R. C., Material tailoring for orthotropic elastic rotating disks, *Composites Science and Technology*, 71(3), 406-414, 2011.

[12] Genta, G., Gola, M., The stress distribution in orthotropic rotating disks, *Journal of Applied Mechanics*, 48(3), 559-562, 1981.

[13] Çallıoğlu, H., Stress analysis of an orthotropic rotating disc under thermal loading, *Journal of Reinforced Plastics and Composites*, 23(17), 1859-1867, 2004.

[14] Eraslan, A. N., Kaya, Y., Varlı, E., Analytical solutions to orthotropic variable thickness disk problems, *Pamukkale University Journal of Engineering Sciences*, 22(1), 24-30, 2016.

[15] El-Naggar, A. M., Abd-Alla, A. M., Fahmy, M.A., Ahmed, S. M., Thermal stresses in a rotating non-homogeneous orthotropic hollow cylinder, *Heat and Mass Transfer*, 39(1), 41-46, 2002.

[16] Haojiang, D., Huiming, W., Weiqiu, C., Transient thermal stresses in an orthotropic hollow cylinder for axisymmetric problems, *Acta Mechanica Sinica*, 20(5), 477-483, 2004.

[17] El-Naggar, A. M., Abd-Alla, A. M., Ahmed, S. M., On the rotation of a non-homogeneous composite infinite cylinder of orthotropic material, *Applied Mathematics and Computation*, 69(2-3), 147-157, 1995.

[18] Abd-Alla, A. M., Mahmoud, S. R., Shehri, N. A., Effect of the rotation on a non-homogeneous infinite cylinder of orthotropic material, *Applied Mathematics and Computation*, 217(22), 8914-8922, 2011.

[19] Zheng, Y., Bahaloo, H., Mousanezhad, D., Vaziri, A., Displacement and stress fields in a functionally graded fiber-reinforced rotating disk with nonuniform thickness and variable angular velocity, *Journal of Engineering Materials and Technology*, 139(3), 031010-10, 2017.

[20] Zenkour, A. M., Allam, M. N. M., On the rotating fiber-reinforced viscoelastic composite solid and annular disks of variable thickness, *International Journal for Computational Methods in Engineering Science and Mechanics*, 7(1), 21-31, 2006.

[21] Tahani, M., Nosier, A., Zebarjad, S. M., Deformation and stress analysis of circumferentially fiber-reinforced composite disks, *International journal of solids and structures*, 42(9-10), 2741-2754, 2005.

[22] Hoffman, O., The brittle strength of orthotropic materials, *Journal of Composite Materials*, 1(2), pp. 200-206, 1967.

[23] Chamis, C. C., Mechanics of composite materials: past, present, and future, *Journal of Composites,Technology and Research*, 11(1), 3-14, 1989.

[24] Chamis, C. C., Simplified composite micromechanics equations for strength, fracture toughness, impact resistance and environmental effects, *Nasa Technical Memorandum (NASA-E-2154)*, Clevland, OH, 1984.

[25] Kaw, A. K., *Mechanics of Composite Materials*, CRC Press; 2nd edition, 2002.

# Investigation of The Effect of Different Prosthesis Designs and Numbers on Stress, Strain and Deformation Distribution

*Gözde Nur Nişanci [a], Yılmaz Güvercin [b], Sabit Melih Ateş [c], Hasan Ölmez [d], Ecren Uzun Yaylacı [e], Murat Yaylacı [f*]*

*[a, f*] Recep Tayyip Erdogan University, Department of Civil Engineering, 53100, Rize, Turkey*
*[b] Recep Tayyip Erdogan University, Department of Orthopaed & Traumatol, 53100, Rize, Turkey*
*[c] Recep Tayyip Erdogan University, Department of Prosthetic Dentistry, 53100, Rize, Turkey*
*[d] Karadeniz Technical University, Department of Marine Engineering Operations, 61530, Trabzon, Turkey*
*[e] Karadeniz Technical University, Surmene Faculty of Marine Science, 61530, Trabzon, Turkey*
*[*]E-mail address*: gozdenurnisanci@hotmail.com [a], yilmaz_guvercin61@hotmail.com [b], melih_ates@hotmail.com [c], hasanolmez@ktu.edu.tr [d], ecrenuzun@ktu.edu.tr [e], murat.yaylaci@erdogan.edu.tr

*ORCID numbers of authors:*
*0000-0002-1976-1948[a], 0000-0003-1861-2083[b], 0000-0001-7137-2096[c], 0000-0001-5351-4046[d], 0000-0002-2558-2487[e], 0000-0003-0407-1685[f*]*

**Abstract**

*Dental implant applications for edentulous jaws are today considered a predictable, safe, and daily technique for giving patients new aesthetics and function. However, the success of the implant therapy should be thoroughly investigated for long-term clinical results about the stress distribution in hosting bone tissue and prosthetic components. In this study, the effect of different prosthesis designs on the stress distribution around the abutment and dental implant in bone tissue was investigated using the finite element method (FEM) with Workbench module of the ANSYS package program. The examination focuses on the effect of the number of implants in teeth layouts on the distribution of stresses, strains, and displacements. In the study the historical development of dental implant problems is mentioned, and some previous studies are summarized. Critical information is also given about biomechanics, dental implants, jawbone, teeth, and the finite element method. Totally four different cases, one layout with three implants and three layouts with two implants, were analyzed. Titanium was used as an implant and abutment material. Nobel Active implants and abutments manufactured by Nobel BioCare Company were used for complete toothless lower jaw case. The critical stress, strain, and displacement values were determined for all four different scenarios. As a result, it was concluded that stresses, strains, and displacements have lower values for the design of triple dental implants compared to other layouts.*

**Keywords:** Biomechanics, Dental implant, Finite element method

## 1. Introduction

Mechanical behaviors of designs that can keep up with the developing technology is one of the main topics of researchers. For this reason, researchers have made analytical and numerical solutions about the mechanical behavior of structures [1-8]. Biomechanics of the respiratory, skeletal, muscular and cardiovascular systems, soft and hard tissues, biological fluids, prosthetics, and tissue-implant interfaces are among the specialized topics of multidisciplinary numerical analysis. In this dental implant treatment process not realistically considering the importance of biomechanical effects may prevent them from continuing their task successfully for a long time and even lead to serious clinical complications.

Dental implant treatments have rapidly increased since the evolution of osseointegration, replacing removable dentures in the treatment of partially edentulous patients. Regardless of the clinician's success, many factors play an important role in load transfer from dental implant to the surrounding bone, such; as loading type, bone-implant integration, length and diameter of the implants, implant surface characteristics, prosthesis design, and quality of the host bone [9]. In the literature, it seen that the relationship between the success or failure of an implant and its useful life with the bone-implant interface has been studied [10]. Factors affecting the balance of implants have been presented and the principles on which implants should be designed for long-term success have been emphasized [11].

In ancient times, it can be counted as a solution for using stone, wood, and animal teeth in the jaw bones instead of a tooth that was lost. Dental implants are the most needed of these kinds of materials and are applied to human jaws in line with the studies performed today. Dental implants are placed under the bony or mucous membrane of the rigid or movable prosthesis, inside the jawbone, to transmit the forces formed between the jaws to the joint points instead of the teeth lost for any reason. Biocompatible materials are used for its production.

Biomechanical behavior analysis are important implications for implants to do their job or not. Failure to apply the occlusal forces in accordance with the real scenarios in calculations poorly affects the stresses at the implant-prosthesis junction and the reshaping of the bone around the implant. Using biomechanical behaviors, which have a significant impact on the life of prostheseis, in this way enables the optimization of biomechanical conditions. There are several methods in the literature to examine stress, strains, and displacements for dental implant analysis. In experimental tests in laboratories, strain measurements give reliable results only at the specific position of the indicator. Photoelasticity provides realistic and reliable information about the global location of stresses, apart from the quantitative values. The finite element analysis is one of the most widely used methods in recent years, not only in the field of engineering but also in the field of dental implants, since it shows the problems that may occur before the application and shows the stresses that it will create around the implant. Geometric designs can be created using the finite element method. Material selection and geometric design are very important in determining the success of dental implants. The finite element analysis (FEA) can provide complete quantitative data at any local location of the model. Therefore, FEA has become a valuable analytical method for numerical analysis of implant applications. Studies on dental implant applications in different cases in the literature can be summarized as follows.

Van Oosterwyck et al. have examined the effects of bone-implant interface, bone mechanical properties, unicortical versus bicortical implant fixation and the presence of a lamina dura by using FEM [10]. Geng et al. have investigated the bone-implant interface, implant prosthesis connection, and its use in multiple implant prostheses [11]. Kunavisarut et al. have aimed to investigate the effect of dental implant-supported passive fit prostheses, cantilever prostheses and various occlusive forces on prostheses, implant components, and stress around the bone using FEM [12]. Ding et al. have aimed to create a 3D FE model of a mandible with dental implants to analyze the stress distribution in the bone around the implants for different diameters [13]. Hsu et al. have studied the application of the finite element analysis in dentistry [14]. Kumar et al. have investigated the stress distribution around implant and tooth the finite element method in implant- supported fixed prosthesis designs [15]. El-Anwar and El-Zawahry have studied 25 different 3D implant designs with a gradual increase in diameter and length in order to extract simplified design equations to better understand implants behavior, using the finite element method [16]. Baggi et al. have compared two different restorative techniques for

complete-arch rehabilitations supported by four implants. [17]. Liu et al. have aimed to evaluate the tension distribution in the peripheral bone, the tension in the abutments and the tension in the abutments, and the prosthetic stability of the mandibular overpressures attached with different implants under different loading conditions [18]. Cicciu et al. has studied the FEM evaluation of cement and screw-held dental implants against a single-tooth crown prosthesis [19]. Hambli has developed a simple and reliable FE model coupled to quasi-brittle damage law to describe the multiple cracks initiation [20]. Parkhe et al. have performed a finite element analysis to determine the best thread shape by comparing stress-induced in cortical and cancellous bone [21]. Gonzalez and Nuno have characterized the three types of manufacturing irregularities on an additive manufactured porous titanium sample having a simple cubic unit-cell using FEA [22]. Mahajan and Patil have studied the optimization of dental implants using FEA [23]. Rzaghi et al. have studied dynamic simulation and the finite element analysis of the maxillary bone injury around the dental implants for different chewing loads [24]. Demenko et al. have estimated implant success prognosis, considering 0.2 mm annual bone loss for successful implantation [25]. Macedo et al. have evaluated the stresses and bone volume of an external hexagon or Morse taper dental implant systems by FEA [26]. Aumnakmanee et al. have studied the effects of four different Thread designs of dental implant prosthetics on stress at four different areas [27]. Jafarian et al. have studied the stress distribution around the implants of different lengths and diameters with the finite element analysis [28]. Wu et al. have evaluated the all-on-four treatment with four osseointegrated implants in terms of the biomechanical effects of implant design and loading position on the implant and surrounding bone using both test results and 3D FEA [29]. Jiménez et al. have used the FEA to determine whether the risks linked to Narrow-diameter implants (NDIs) could be mitigated by the mechanical advantages [30]. Robau Porrua et al. have examined the effect of the diameter, length, elasticity module on a dental implant on the stress and strain distribution in the implant bone by 3D FEA [31]. Zhong et al. have analyzed the biomechanical responses of zirconia-based FAFDPs with different implant configurations by using the FEM [32]. The effect of different abutment materials on the stress distribution in bone tissue around the dental implant has investigated using the FEM by Terzi et al. [33].

Biomechanical principles help to evaluate existing designs in dental implantology and to model new designs. The FEM has been adapted from the engineering field to the dental implantology for an approximate prediction and evaluation of the amount of stress that will occur on the implant or surrounding tissues during the function performed. The finite element method is a method that explains the complex biomechanics of the implant studied and provided numerical results. In this study, it was aimed to find the stress, strain, and displacement values of the dental implants with different geometrical structures by changing the number of implants in four different strategies.

## 2. Finite Element Analysis

In this section, *a* 3.9 *mm* diameter prosthesis system is designed on bone tissue taken from a healthy person and this prosthesis is mounted. The geometry of the underlying system is introduced. The prosthesis and abutment system designed on the obtained bone tissue is connected under the first minor molar-second minor molar and first major molar teeth. Solidworks program was used to create the geometry [34]. After the design of the 3D model, the FEM was used for analysis. Stress, strain and displacement values were compared on the model by changing the selected material on the same model. In this study, the ANSYS Workbench program was used for the finite element analysis [35].

The first step to be taken when starting the finite element analysis is to create a three-dimensional model of the object to be worked on. While preparing these models, different imaging methods can be used depending on the complexity of the object. Computerized tomography and magnetic resonance imaging methods are two examples. While transferring such images to the computer environment and creating the model, firstly real models are created by scanning each detail of the object with 3D scanners and transferred to the computer environment or drawn by the researcher with three-dimensional modeling programs. The desired results can be simulated through the mathematical model and test simulations can be repeated at any time. Therefore, a well-tested and validated mathematical model offers researchers a very powerful tool for analysis.

The geometric model prepared in the finite element analysis is divided into simple geometric infrastructures called elements, which are classified according to certain features. As some example of these features, geometric shape (triangle, parallel edge, quadrilateral), size (one-dimensional, two-dimensional, three-dimensional) and the number of nodes can be given. Element types are shown in Figure 1. These elements are fully compatible with the geometry of the existing main structure. They show the desired mechanical properties in each region of the main structure.
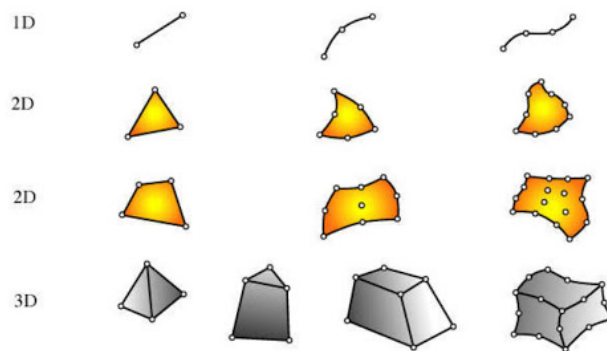


Fig. 1. Finite element types (one-dimensional, two-dimensional and three-dimensional)

After the desired model is transferred to the computer environment, the division of the elements is called the creation of a network structure. The model analysis can be made in the most realistic way and reduced to a simpler model. Corner contact points between the elements are called knot points. In the second step, material data such as elasticity modulus, Poisson ratio used material are defined in the program. The boundary conditions of the object and the forces applied to the object are defined in the third step of the analysis. After entering this information, the analysis is performed by adjusting the direction, intensity and angle of the force for the loading conditions to be applied to the object. As a result of the solution, the sub-elements of each object and the entire structure are evaluated. In the interpretation of the analysis made using the finite element method, the values that directly affect the results of the analysis are chosen. These are, the geometry of the bone and implant, material properties, boundary conditions, force properties, and properties of the implant-bone interface.

In this study, the finite element analysis was performed by transferring dental implant, abutment and lower jawbone modeling from Solidworks to the ANSYS Workbench program. The computerized tomography image of the bone tissue simplified and modeled to the desired extent is shown in Figure 2.
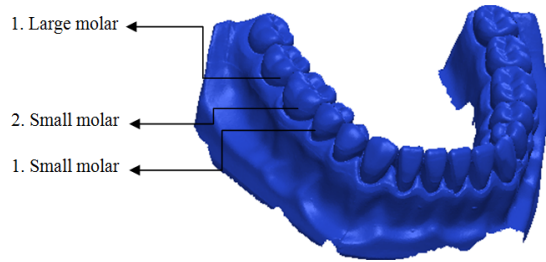
Fig. 2. Created solid modeling of the prosthesis

The bone tissue image obtained by computerized tomography has been reduced to a simpler model by Solidworks program. As seen in Figure 3-b, the *3.9 mm* diameter and 13 mm length dental implant of the Nobel Biocare Company named the Nobel Active which provides excellent stability in all areas was created by the Solidworks program. In Figure 3-c, a suitable custom abutment (personalized application) designed according to the dental implant solid model is shown in Figure 3.
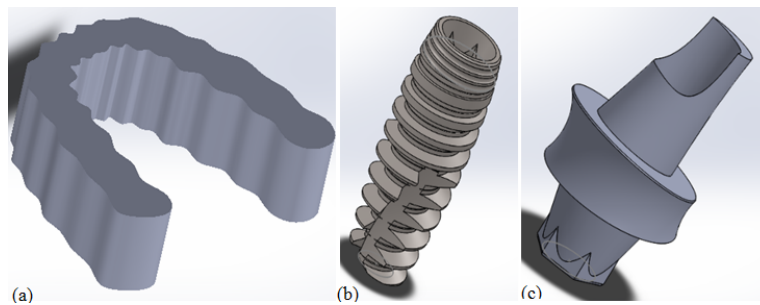


Fig. 3. (a) Bone modeling (b) Dental implant modeling (c) Abutment modeling

Layouts have been created for assembly operations and listed as follows in Figure 4. In this section, different geometrical assemblies of prosthetic systems designed with a diameter of *3.9 mm* and abutment systems of which the assemblies made are described. Prosthesis and abutment systems designed on the resulting bone tissue are linked under teeth as the following designs;

Model 1: 1. small molar, 2. small molar, and 1. large molar
Model 2: 1. small molar, and 1. large molar
Model 3: 1. small molar, and 2. small molar
Model 4: 2. small molar, and 1. large molar
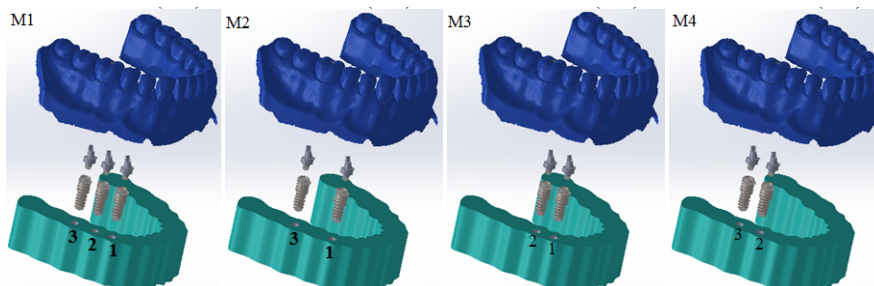


Fig. 4. Assembly layouts

After the solid model of each part were created, they were transferred to the assembly stage. Bone, dental implants and abutments are combined by placing them in suitable positions for assembly. Firstly, the mandible and dental implants were created in the SolidWorks software and then transferred to the ANSYS Workbench program for the analysis, as shown in Figure 5.
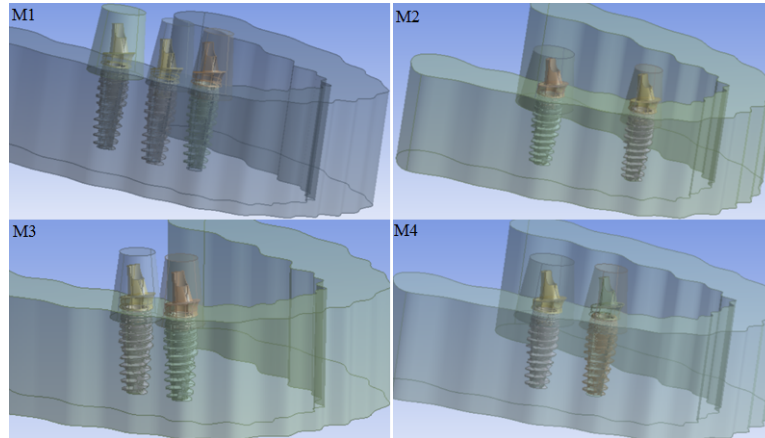
Fig. 5. Imported geometry for ANSYS Workbench

The solid model was transferred to the ANSYS Workbench program for numerical solution. The data that must be entered into the system to perform the analysis are introduced one by one. Young's modulus and Poisson ratios are taken from the literature. The data used in the study are shown in Table 1.

Table 1. The material properties of the models

|          | Materials | Modulus of elasticity (*MPa*) | Poisson's ratio | Literature |
|----------|-----------|-------------------------------|-----------------|------------|
| Abutment | Ti6Al4V   | 113800                        | 0.34            | [36]       |
| Implant  | Ti6Al4V   | 113800                        | 0.34            | [36]       |
| Bone     | Bone      | 14000                         | 0.30            | [37]       |

In Figures 6-7, the mesh structure of the solid model on ANSYS Workbench is given. 191622 elements and 321422 nodes are used in the model. After the mesh structure was created, 50 N load was applied to the abutments.
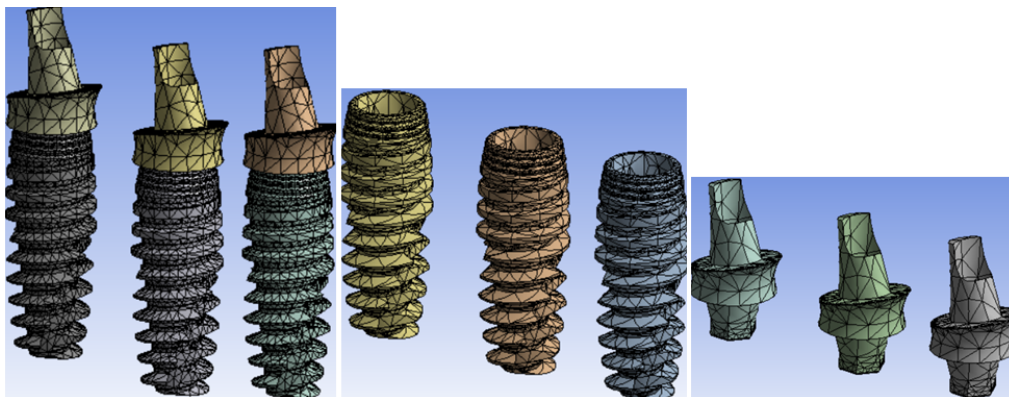


Fig. 6. 3D mesh of the dental implant and abutment
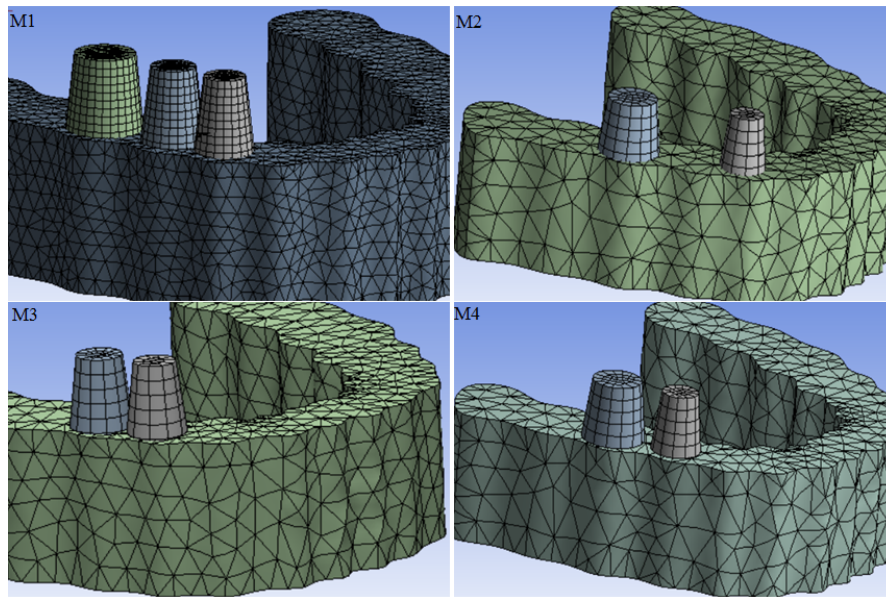
Fig. 7. 3D mesh of the structure

Three different models with two implants and one model with three implants were created. Three different teeth were applied to the models, namely the first molars, the second molars and the third molars. Titanium was chosen and used as a dental implant material. Static structural stress analysis was performed for the models. After all the necessary data such as boundary conditions and loads are defined in the ANSYS Workbench software, the analysis phase has been started and the obtained results are described in the numerical results part. Results of four different models under *50 N* load are given below.

## 3. Numerical Results

In this study, the finite element method was used to obtain stress, strain, and deformation values in each region of the bone, dental implant, and abutment. Titanium was used as a dental implant, and abutment material for all models. The stress, strain, and displacement images and numerical values of the analysis results for the Model 1 (M1), Model 2 (M2), Model 3 (M3), and Model 4 (M4) are shown in Figures 8-10 and Tables 2-5, respectively.

The stress, strain, and displacement images and numerical values of the analysis results for the bone are shown in Figure 8 and Table 2, respectively. As can be seen from the table, the highest stress values were obtained in the M2, the highest strain values were obtained in the M4, and the highest deformation values were obtained in the M3. The lowest stress values were obtained in the M1, the lowest strain values were obtained in the M1 and the lowest deformation values were obtained in the M2.
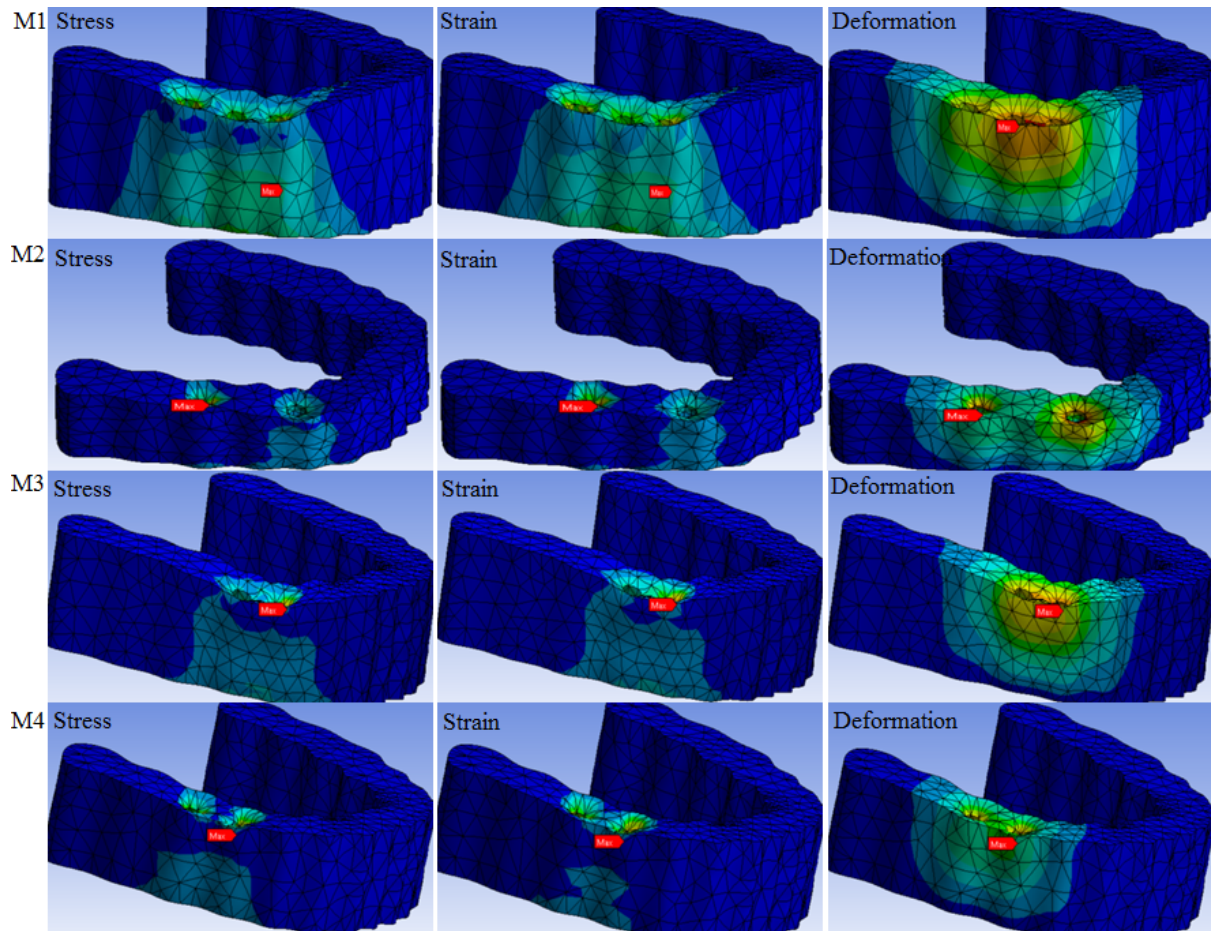
Fig. 8. Analysis images of the stress, strain, and deformation in the bone

Table 2. Results of the stress, deformation, and displacement in the bone

| Models | Max. Von-Mises Stress (MPa) | Max. Strain $(10^{-4})$ | Max. Deformation (mm) $(10^{-4})$ |
|--------|------------------------------|--------------------------|-----------------------------------|
| M1 | 1.3981 | 1.0144 | 7.4699 |
| M2 | 2.4186 | 1.8684 | 5.8766 |
| M3 | 2.4093 | 1.7773 | 7.5332 |
| M4 | 2.2610 | 2.0067 | 7.4385 |

The stress, strain, and displacement images and numerical values of the analysis results for the dental implants are shown in Figure 9 and Table 3, respectively. As can be seen from the table, the highest stress values for the first, second, and third dental implants were obtained in the M1, M4 and M4 respectively. The highest strain values for the first, second, and third dental implants were obtained in the M1, M4, and M4. The highest deformation values for the first, second, and third dental implants were obtained in the M3, M4, and M4. As can be seen from the table, the lowest stress values for the first, second, and third dental implants were obtained in the M2, M1 and M1 respectively. The lowest strain values for the first, second, and third dental implants were obtained in the M2, M1, and M1. The lowest deformation values for the first, second, third dental implants were obtained in the M2, M3, and M1.
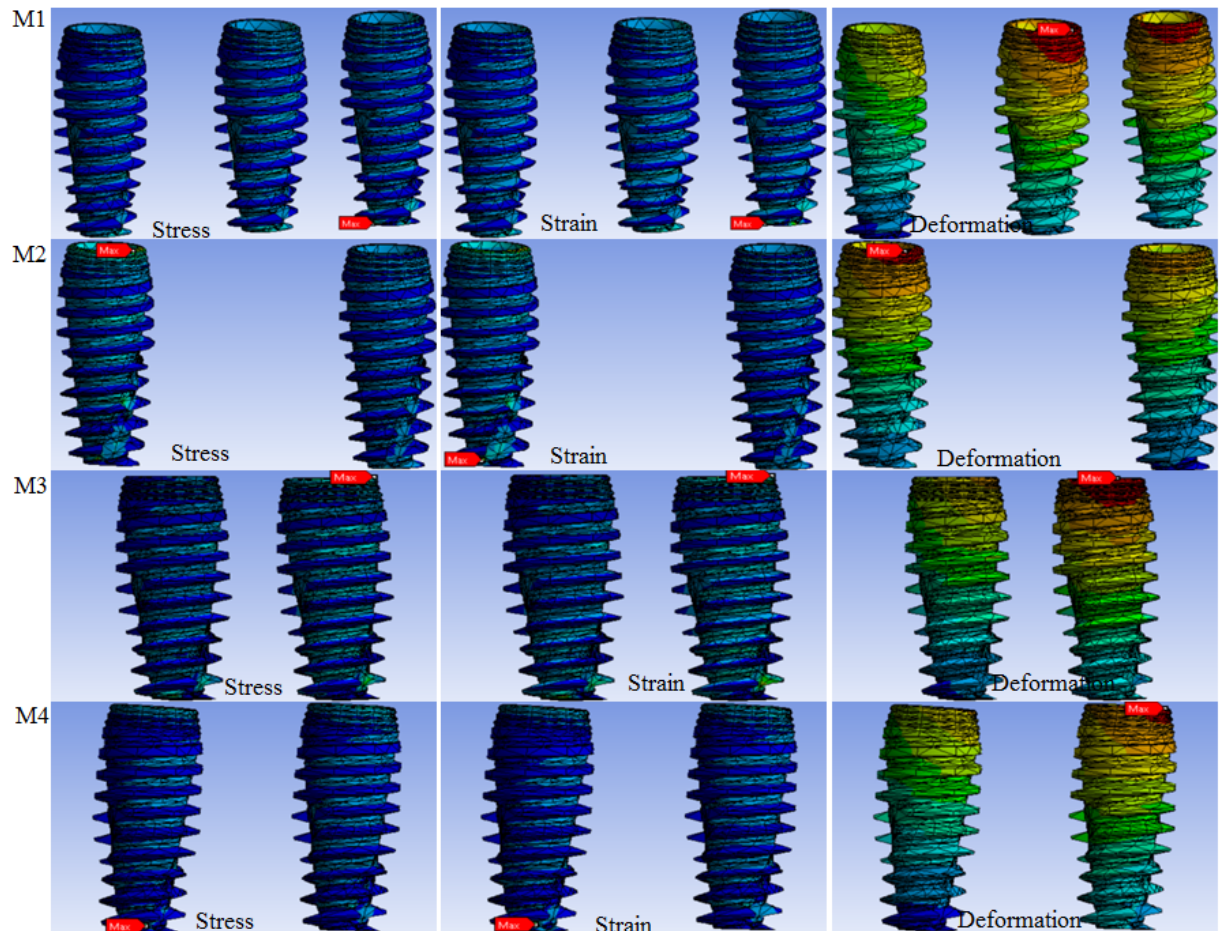
Fig. 9. Stresses, strains and deformations in the dental implants

Table 3. Results of the stress, deformation, and displacement in the implants

| **First Dental Implant** | | |
|---|---|---|
| **Models** | **Max. Von-Mises Stress (MPa)** | **Max. Strain ($10^{-4}$)** | **Max. Deformation (mm) ($10^{-4}$)** |
| M1 | 16.7090 | 1.5345 | 7.0567 |
| M2 | 7.0089 | 0.6488 | 5.4778 |
| M3 | 16.3770 | 1.4900 | 7.8450 |
| M4 | - | - | - |
| **Second Dental Implant** | | |
| **Models** | **Max. Von-Mises Stress (MPa)** | **Max. Strain ($10^{-4}$)** | **Max. Deformation (mm) ($10^{-4}$)** |
| M1 | 8.8032 | 0.8147 | 7.3773 |
| M2 | - | - | - |
| M3 | 14.0200 | 1.3748 | 6.8087 |
| M4 | 15.9690 | 1.5023 | 7.5063 |
| **Third Dental Implant** | | |
| **Models** | **Max. Von-Mises Stress (MPa)** | **Max. Strain ($10^{-4}$)** | **Max. Deformation (mm) ($10^{-4}$)** |
| M1 | 9.6161 | 0.9130 | 6.1572 |
| M2 | 17.0410 | 1.7195 | 6.1651 |
| M3 | - | - | - |
| M4 | 26.7020 | 2.6432 | 6.5491 |

The stress, strain and displacement images and numerical values of the analysis results for the abutment are shown in Figure 10 and Table 4, respectively. As can be seen from the table, the highest stress values for the first, second, and third abutments were obtained in the M1, M4, and M4 respectively. The highest strain values for the first, second, and third abutments were obtained in the M1, M4, and M4. The highest deformation values for the first, second, and third abutments were obtained in the M3, M4, and M4. As can be seen from the table, the lowest stress values for the first, second, and third abutments were obtained in the M3, M3, and M1 respectively. The highest strain values for the first, second, and third abutments were obtained in the M3, M3, and M1. The highest deformation values for the first, second, and third abutments were obtained in the M2, M3, and M1.
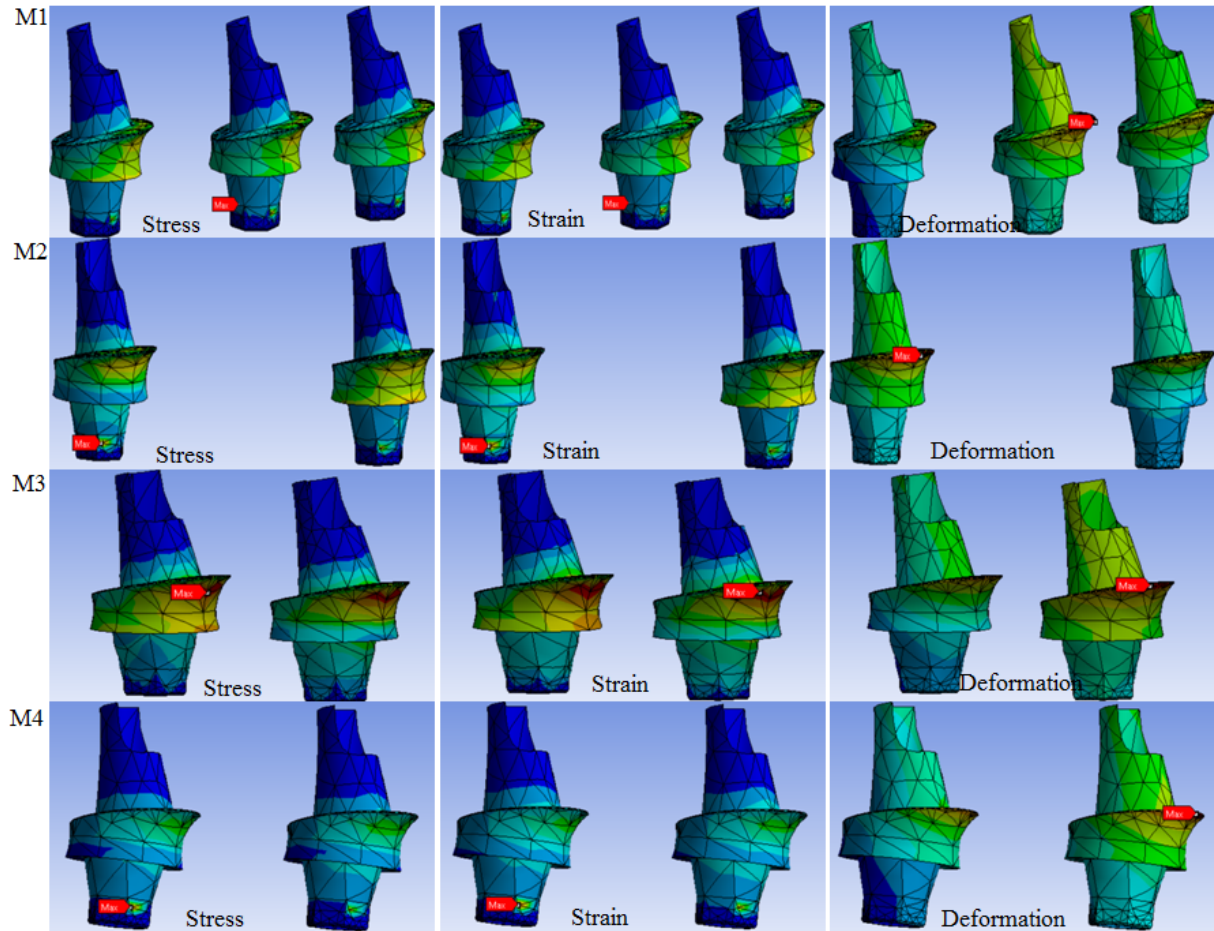


Fig. 10. Stresses, strains, and deformations in the abutments

Table 4. Results of the stress, deformation, and displacement in the abutments

| **First Dental Implant** | | | |
|---|---|---|---|
| **Models** | **Max. Von-Mises Stress (MPa)** | **Max. Strain (10⁻⁴)** | **Max. Deformation (mm) (10⁻⁴)** |
| M1 | 11.1670 | 1.1098 | 9.5823 |
| M2 | 10.2530 | 0.9523 | 8.3830 |
| M3 | 9.2542 | 0.8634 | 11.0920 |
| M4 | - | - | - |
| **Second Dental Implant** | | | |
| **Models** | **Max. Von-Mises Stress (MPa)** | **Max. Strain (10⁻⁴)** | **Max. Deformation (mm) (10⁻⁴)** |
| M1 | 11.9320 | 1.1721 | 10.6140 |
| M2 | - | - | - |
| M3 | 9.2966 | 0.8609 | 10.1660 |
| M4 | 12.5810 | 1.2684 | 10.6880 |
| **Third Dental Implant** | | | |
| **Models** | **Max. Von-Mises Stress (MPa)** | **Max. Strain (10⁻⁴)** | **Max. Deformation (mm) (10⁻⁴)** |
| M1 | 10.5810 | 1.0424 | 9.4376 |
| M2 | 12.0060 | 1.1913 | 9.5851 |
| M3 | - | - | - |
| M4 | 17.6070 | 1.7118 | 10.0410 |

According to Figures 11-13, it is seen that the stress values of bone are close to each other for M1, M2, M3 and M4 models, but it has a lower value when using M1. In dental implants, the stress values are found different for the first, second and third dental implants in all models. The stress values in the first and third dental implant are higher than the second implant. The stress values for abutments are close to each other for all models. Maximum Von-Mises stress values for all abutments were obtained when using M4, while minimum stresses were obtained when using M2.

As can also be seen from the data in Figures 11-13, the highest value of strain in bone and dental implants was obtained when using M4, and the lowest value of strain was obtained when using M1. The maximum strain values for the abutments were obtained when Model 4 was used as the design.

When the numerical data in Figures 11-13 are examined, it is seen that the results obtained using M1, M2, M3, and M4 designs were close to each other. The maximum deformation values were obtained when using M3 in bone, dental implants and abutments, while the lowest values were obtained in M2.

When all the results were examined, the lowest stress, strain and deformation results among the analyzed design were generally seen in the M1. As a result, it is possible to say that the most suitable model among these for models is the M1.
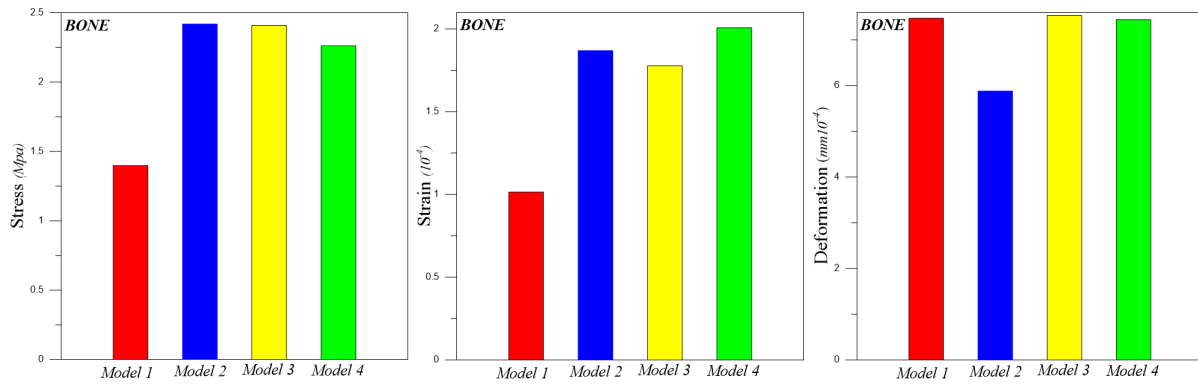
Fig. 11. Stresses, strains, and deformations in the bone
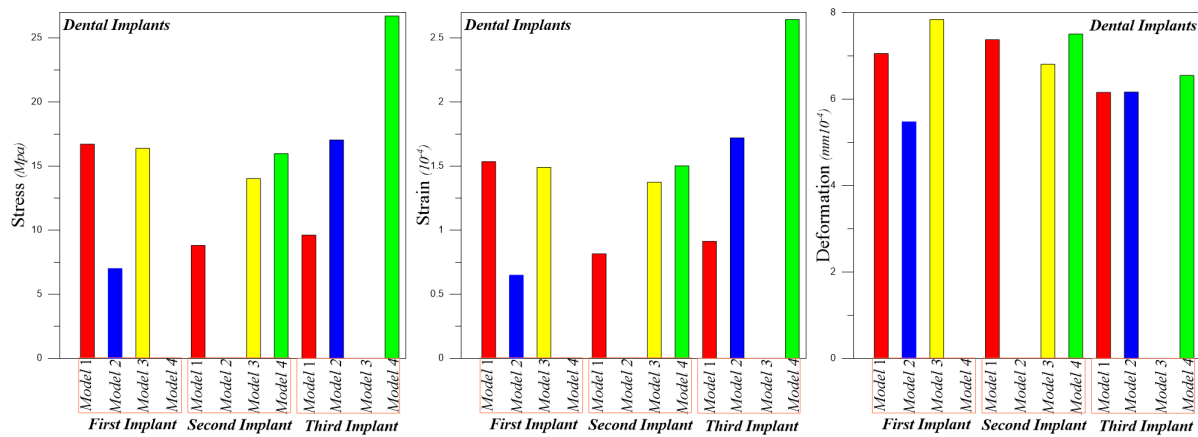


Fig. 12. Stresses, strains, and deformations in the dental implants
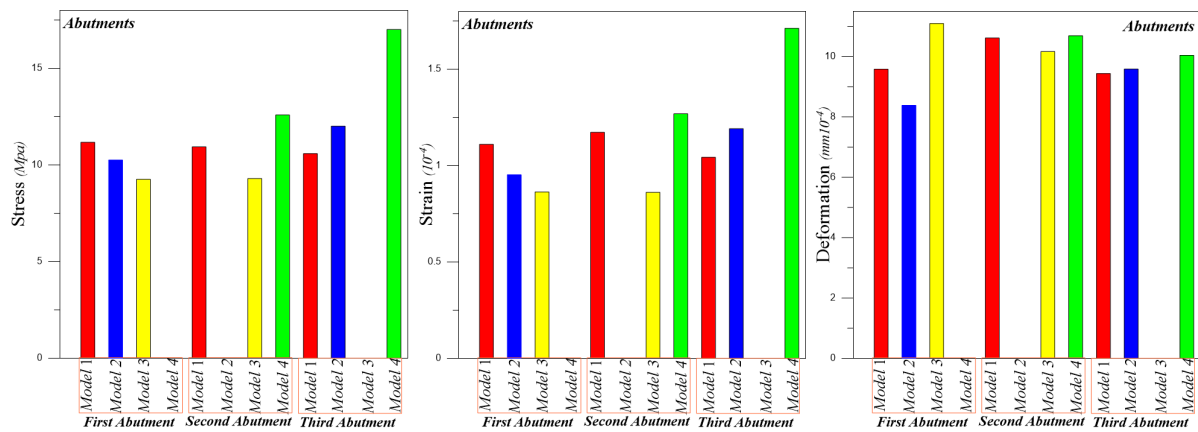


Fig. 13. Stresses, strains, and deformations in the abutments

## 4. Conclusion

In the study, the stress, strain and deformation that were formed as a result of supporting dental implant supported prostheses with three and two implants in different locations and with a single type of implant material were examined. Three models with two implants and one model with three implants were created as a dental implant layout. The obtained models are analyzed

149

with the help of the ANSYS Workbench finite element program. The results are described below.

1. The stress values occurring in three implant models were lower than the two implant models for all loading conditions. The reason for this may be that the applied force is shared by three implants.

2. The maximum Von-Mises stress, strain and deformation values occurring in two implant models differed by the change in the region of the implant location and the applied load. For example, in Model 2, maximum stress, strain and deformation results are from the application of the load to the first molars, whereas in Model 3, the first molar tooth is in the first molar tooth, while in Model 4 the stress and strain values are in the first molar tooth. The replacement value was observed to occur in the second premolar tooth.

3. The stresses occurring in the implants are concentrated in the implant neck region and reached the highest strain values at the implant neck point. The channels located in the implant neck region and which allow the implant to fit better in the bone caused the initial loading to be covered by the implant neck region and the region where the maximum stress values were observed.

4. The stresses, deformations, and total displacements occurring in the abutments are concentrated in the abutment step region and the highest values are also formed in this region.

5. When the stress values occurring in the bone were examined, the highest values occurred in the hard bone layer.

6. Decrease in the number of implants caused negative biomechanical behavior for all structures (M2, M3, M4).

7. Considering two implant-supported prostheses, Model 2 showed that stress and strain distributions were more suitable.

8. The use of fixed showed unwanted biomechanical behavior for M3 and M4, mainly for M4.

9. The use of three implants gave lower results of stress and strain.

10. Considering two implant-supported prostheses, M3 and M4 showed unwanted biomechanical behavior, especially for M4.


## References

[1] Uzun, B. and Civalek, O., Nonlocal FEM formulation for vibration analysis of nanowires on elastic matrix with different materials, *Mathematical and Computational Applications*, 24, 38, 2019.

[2] Jalaei, M. and Civalek, Ö., On dynamic instability of magnetically embedded viscoelastic porous FG nanobeam, *International Journal of Engineering Science*, 143, 14-32, 2019.

[3] Civalek, O., Uzun, B., Yaylı, M.O. and Akgöz, B., Size-dependent transverse and longitudinal vibrations of embedded carbon and silica carbide nanotubes by nonlocal finite element method, *European Physical Journal Plus*, 135, 381, 2020.

[4] Civalek, Ö. and Demir, C., A simple mathematical model of microtubules surrounded by an elastic matrix by nonlocal finite element method, *Applied Mathematics and Computation*, 289, 335-352, 2016.

[5] Gurses, M., Akgoz, B. and Civalek, O., Mathematical modeling of vibration problem of nanosized annular sector plates using the nonlocal continuum theory via eight-node discrete singular convolution transformation, *Applied Mathematics and Computation*, 219, 3226- 3240, 2012.

[6] Yaylaci, M. and Avcar, M., Finite element modeling of contact between an elastic layer and two elastic quarter planes, *Computers and Concrete*, 26(2), 107-114, 2020.

[7] Yaylaci, M., Terzi, C. and Avcar, M., Numerical analysis of the receding contact problem of two bonded layers resting on an elastic half plane, *Structural Engineering and Mechanics*, 72(6), 775-783, 2019.

[8] Yaylacı, M., Bayrak, M.Ç. and Avcar, M., Finite element modeling of receding contact problem, *International Journal of Engineering and Applied Sciences,* 11(4) 468-475, 2019.

[9] Chen, J., Ahmad, R., Suenaga, H., Li W., Swain, M. and Li Q., A comparative study on complete and implant retained denture treatments – A biomechanics perspective, *Journal of Biomechanics*, 48(3), 512-519, 2015. https://doi.org/10.1016/j.jbiomech.2014.11.043.

[10] Van Osterwyck, H., Duyck, J., Vander, S., Vander, P.G., Decoomans, M., Lieven, S., Puers, R. and Naert, L., The influence of bone mechanical properties and implant fixation upon bone loading around oral implants, *Clin Oral Implants Res*, 9(6), 407-412, 1998. https://doi.org/10.1034/j.1600-0501.1996.090606.x

[11] Geng, J.P., Tan, K.B. and Liu, G.R., Application of finite element analysis in implant dentistry: a review of the literature, *Journal of Prosthetic Dentistry,* 85(6), 585-98, 2001. https://doi.org/ 10.1067/mpr.2001.115251.

[12] Kunavisarut, C., Lisa, A.. Lang, L.A., Stoner, B.R. and Felton, D.A., Finite element analysis on dental implant- supported prostheses without passive fit, *Journal of Prosthodontics*, 11(1), 30-40, 2002. https://doi.org/ 10.1111/j.1532-849x.2002.00030.x.

[13] Ding, X., Zhu, X.H., Liao, S.H., Zhang, X.H. and Chen, H., Implant–Bone interface stress distribution in immediately loaded implants of different diameters: a three-dimensional finite element analysis, *Journal of Prosthodontics*, 18, 393–402, 2009. https://doi.org/ 10.1111/j.1532-849X.2009.00453.x.

[14] Hsu, M.L. and Chang, C.L., Application of finite element analysis in dentistry, *Finite Element Analysis*, 5, 43-6, 2010.

[15] Kumar, G.A., Kovoor, L.C. and Oommen, V.M., Three-dimensional finite element analysis of the stress distribution around the implant and tooth in tooth implant- supported fixed prosthesis designs, *Journal of Dental Implants*, 1(2), 75-79, 2011.

[16] El-Anwar, M.I. and El-Zawahry, M.M., A three-dimensional finite element study on dental implant design, *Journal of Genetic Engineering and Biotechnology*, 9(1), 77-82, 2011. https://doi.org/10.1016/j.jgeb.2011.05.007.

[17] Baggi, L., Pastore, S., Girolamo, M.D. and Vairo, G., Implant-bone load transfer mechanisms in complete-arch prostheses supported by four implants: A three-dimensional finite element approach, *The Journal of Prosthetic Dentistry*, 109(1), 9-21, 2013.

[18] Liu, J., Pan, S., Dong, J., Mob, Z., Fan, Y. and Feng, H., Influence of implant number on the biomechanical behavior of mandibular implant-retained / supported overdentures: A three-dimensional finite element analysis, *Journal of Dentistry*, 41, 241-249, 2013.

[19] Cicciu, M., Bramanti, E., Cecchetti, F., Scappaticci, L., Guglielmino, E. and Risitano, G., FEM and Von Mises analyses of different dental implant shapes for masticator loading distribution, *Oral&Implantology,* 1, 1-10, 2014.

[20] Hambli, R., 3D finite element simulation of human proximal femoral fracture under quasi-static load, *Biomaterials and Biomechanics in Bioengineering,* 1(4), 175-188, 2016. http://dx.doi.org/10.12989/bme.2014.1.4.175.

[21] Parkhe, N., Hambire, U., Hambire, C. and Gosavi, S., Enhancing dental implant model by evaluation of three-dimensional finite element analysis, *International Journal of Engineering Science Invention*, 4(12), 26-33, 2015.

[22] Gonzalez, F.J.Q. and Nuno, N., Finite element modeling of manufacturing irregularities of porous materials, *Biomaterials and Biomechanics in Bioengineering*, 3(1), 1–14, 2016. https://doi.org/10.12989/BME.2016.3.1.001.

[23] Mahajan, S. and Patil, R., Application of finite element analysis to optimizing dental implant, *International Research Journal of Engineering and Technology,* 3(2), 850-856, 2016.

[24] Razaghi, R., Mallakzadeh, M. and Haghpanahi, M., Dynamic simulation and finite element analysis of the maxillary bone injury around dental implant. biomedical engineering: applications, *Basis and Communications*, 28(2), 1-10, 2016.

[25] Demenko, V., Linetskiy, I., Linetska, L., Nesvit, V., Shevchenko, A., Yefremov, O. and Weisskircher, H.W., Prognosis of implant longevity in terms of annual bone loss: a methodological finite element study, *Computer Methods in Biomechanics and Biomedical Engineering*, 19(2), 180-187, 2016. https://doi.org/ 10.1080/10255842.2015.1005079.

[26] Macedo, J.P., Pereira, J., Faria, J., C.A. Pereira, J., Alves, L., Henriques, B., Souza, J.C.M. and López-López, J., Finite element analysis of stress extent at peri-implant bone surrounding external hexagon or Morse taper implant, *Journal of the Mechanical Behavior of Biomedical Materials*, 71, 441-447, 2017. https://doi.org/ 10.1016/j.jmbbm.2017.03.011.

[27] Aumnakmanee, S., Yodpiji, N., Jantong, N. and Jongprasithporn, M., Finite element analysis of dental implant prosthetic, *Materials Today: Proceedings*, 5, 9525–9534, 2018. https://doi.org/10.1016/j.matpr.2017.10.134.

[28] Jafarian, M., Mirhashemi, F.S. and Emadi, N., Finite element analysis of stress distribution around a dental implant with different amounts of bone loss: An in vitro study, *Dental and Medical Problems*, 56(1), 27-32, 2019. https://doi.org/ 10.17219/dmp/102710.

[29] Wu, A.Y.J., Hsu, J.T., Fuh, L.J. and Huang, H.L., Biomechanical effect of implant design on four implants supporting mandibular full-arch fixed dentures: In vitro test and finite element analysis, *Journal of the Formosan Medical Association*, 4, 1-10, 2019. https://doi.org/ 10.1016/j.jfma.2019.12.001.

[30] Jimenez, V.J.F., Burgueno-Barris, G., Gomez-Gonzalez, S., Lopez-Lopez, J., Valmaseda-Castellon, E. and Fernandez-Aguado. E., Finite element analysis of narrow dental implants, *Dental Materials*, 36(7), 927-935, 2020.

[31] Robau Porrua, A., Perez Rodriquez, Y., Soris Rodriquez, L.M. and Perez Acosta, O., The effect of diameter, length and elastic modulus of a dental implants on stress and strain levels in peri-implant bone: A 3D finite element analysis, *Bio-Medical Materials and Engineering*, 30, 541-558, 2020. https://doi.org/ 10.3233/bme-191073.

[32] Zhong, J., Guazzato, M., Chen, J., Zhang, Z., Sun, G., Huo, X., Liu, X., Ahmad, R. and Li, Q., Effect of different implant configurations on biomechanical behavior of full-arch implant-supported mandibular monolithic zirconia fixed prostheses, *Journal of the Mechanical Behavior of Biomedical Materials*, 102, 1-10, 2020. https://doi.org/ 10.1016/j.jmbbm.2019.103490.

[33] Terzi, M., Güvercin, Y., Ateş, S.M., Sekban, D.M. and Yaylacı M., Effect of different abutment materials on stress distribution in peripheral bone and dental implant system, *Sigma Journal of Engineering and Natural Sciences*, 38(3), 1495-1507, 2020.

[34] Solidworks 2018, (2018). Dassault Systèmes Solidworks Corporation. Waltham MA, USA.

[35] ANSYS 16.0, (2016). Swanson Analysis Systems Inc., Houston PA, USA.

[36] Wadatkar, N.D., Londhe, S.D. and Metkar R.M., Stress analysis of fractured femur bone and implant of different metallic biomaterials, *Trends in Biomaterials and Artificial Organs*, 34(3), 96-99, 2020.

[37] Korkmaz, H.H., Evaluation of different miniplates in fxation of fractured human mandible with the finite element method, *Oral Surg Oral Med Oral Path Oral Radiol Endod*, 103(6), 1-13, 2007.

# Size Dependent Buckling Analysis of Hybrid Organic/Inorganic Nano-Sized I-Beam

*Kadir Mercan*

*Burdur Mehmet Akif Ersoy University, Engineering and Architecture Faculty, Civil Engineering Department, Burdur, Turkey*
*E-mail address*:  kmercan@mehmetakif.edu.tr

*ORCID numbers of authors:*
*0000-0003-3657-6274*

## Abstract

*In the paper, the size dependent buckling analysis of hybrid organic/inorganic nanobeam with I cross section is investigated. Eringen's nonlocal elasticity theory is used to take the size effect into consideration. Comparative buckling loads of nanobeams for first ten modes is plotted in figure using Euler-Bernoulli theory and Eringen's nonlocal elasticity theory. Two different size parameter is used. It is clearly demonstrated that the size effect can be neglected for first modes while it is unneglectable for higher modes. Simply supported case in investigated. The advantages of I-cross section are discussed.*

**Keywords:** Nonlocal elasticity theory, Euler-Bernoulli, Hybrid nanobeam, Nano-sized I-beam.

## 1. Introduction

Nano sized materials attracted much attention because of their out of the common properties. The starting point of the rise of these materials is the discovery of Carbon Nanotubes (CNTs) by Iijima in 1991 [1]. CNTs are graphene based materials. The discovery of graphene happened 13 years later of CNTs [2]. Many methods of obtaining CNTs from graphene sheets was developed (layer separation, chemical separation, chemical vapor deposition etc.). The key point of attracting much attention is the material was performing outstanding mechanical strength, electronical conductivity, physicochemical properties compared to any known material [3]. Working experimentally with CNTs need advanced level of laboratory equipment together with very high experiment cost. Also, researchers have fronted to working theoretically instead of experiments because of time. A researcher can obtain results for thousands of alternative variant in seconds while working theoretically using accurate models [4]. As nanotubes dimensions are in nanometer level, classical theories were insufficient to perform theoretic analysis [5]. In past years, researchers developed and proved the accuracy of new size-dependent theories such as nonlocal elasticity [6, 7], strain gradient [8, 9], modified couple stress [10], surface elasticity [11-13] theories to perform modal [14-25], bending [26-28], buckling [29-35] analyzes accurately. In more detail some other outstanding properties of these materials can be stated as high energy absorption, very high strength, superior electrical conductivity, flexibility, high maximum current density, high thermal conductivity, reduced skin and proximity effect, extreme lightweight, fatigue resistance etc. CNTs are performing very well in supercapasitors which are widely applied in portable devices, electric vehicles [36],

drug delivery [37], high-strength polymer compounds, water-gas shift and production of $H_2$ [38]. Lately, with the rise of popularity and extremely widened usage area CNTs and functionally graded materials (FGMs) are composed to create a novel type of composite material [39-50]. The novel composed material is named functionally graded carbon nanotube-reinforced composites (FG-CNTRC) [51]. FG-CNTR has both advantages of CNTs and FGMs [52-55]. However, CNTs are not performing drastic mechanical strength or electrical or thermal conductivities for many applications [56]. The load capacity of CNTs and its composites started to be insufficient for some specific area. Therefore, scientists aimed to develop the classical tubular CNT structure [57]. Elmoselhy [58] presented a molecular form of I-shaped like beam CNT. The web resists shear forces applied to nanostructure, while the flanges resist most of the bending moment. The I shaped structure have advantages in carrying both bending and shear loads in the plane of the web while having the disadvantage of reduced capacity in the transverse direction, and carrying torsional loads. In present work, the buckling analysis of I-shaped hybrid nanobeam is investigated. In order to take the size effect into consideration, Eringen's nonlocal elasticity theory is used.

## 2. Hybrid Organic/Inorganic Nano-Sized I-Beam

The classical method of obtaining conventional nanotubes with tubular cross section is demonstrated in Fig. 1. As it can be seen clearly from Fig. 1, the graphene-like flat structure composed of Carbon atoms, Silicon and Carbon atoms, Boron and Nitrogen atoms bonded to each other for obtaining CNTs, silicon carbide nanotubes (SiCNTs), and boron nitride nanotubes (BNNTs) respectively by simply rolling it to form the tubular structure [59].
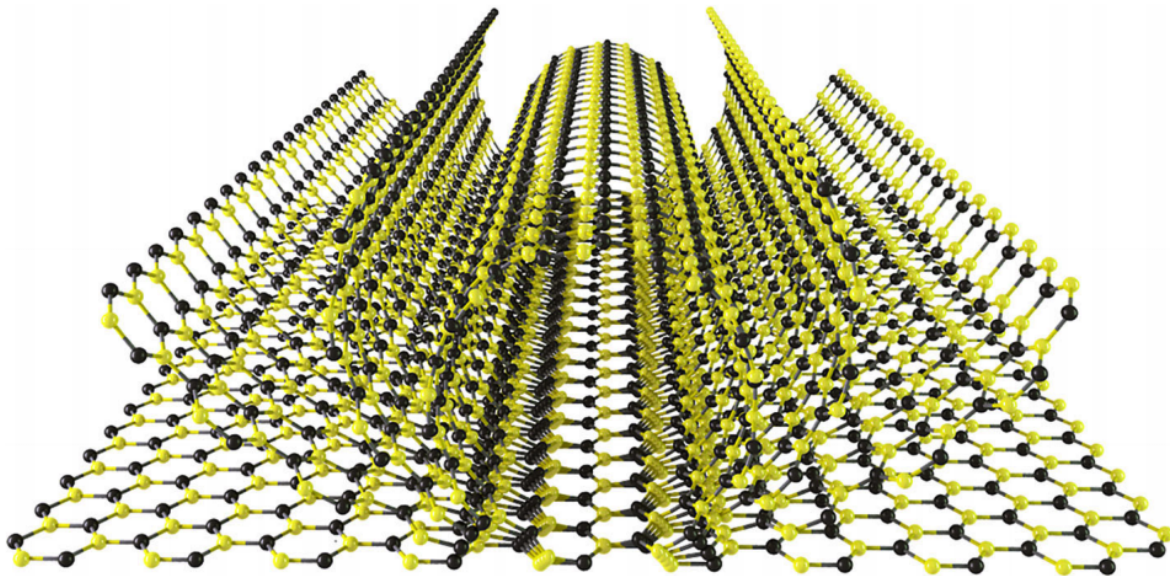


Fig. 1. Obtaining nanotube from graphene-like structure [60]

The discovery and usage of inorganic nanotubes is later than organic nanotubes. Inorganic nanotubes are synthesized of group III-Nitrides, metal oxides, or other inorganic elements. Inorganic nanotubes have the advantages in case of ease in synthesis, high crystallinity, uniformity, high impact-resistance, high chemical stability under acidic and basic conditions [61]. Obtaining nanobeam with I shaped cross section was described by Elmoselhy [58]. Unlike the conventional techniques, a hybrid growth method was used. In the method, perpendicular growing technique of nanorods was combined with a tangential growing technique of a ribbon

of multi nanorods. Five phases of of growing were used to form a nanoribbon which compose the flange of the single walled nano-sized I-beam. Discrete catalytic nanoparticle (Inorganic $Fe_2O_3$) was placed on substrate, then chemical vapor deposition method was used to obtain hybrid organic/inorganic nano-sized I-Beam. It is also demonstrated that different I cross-sectioned alternative nanobeams can be obtained according to the need in usage area. Alternative structures are single walled hollow, single walled solid, multi-walled hollow, multi-walled solid nano-I-beams. In Fig. 2, the obtained nano-sized beam with I cross section is demonstrated. Selected nano I-beam is single walled solid nanobeam.
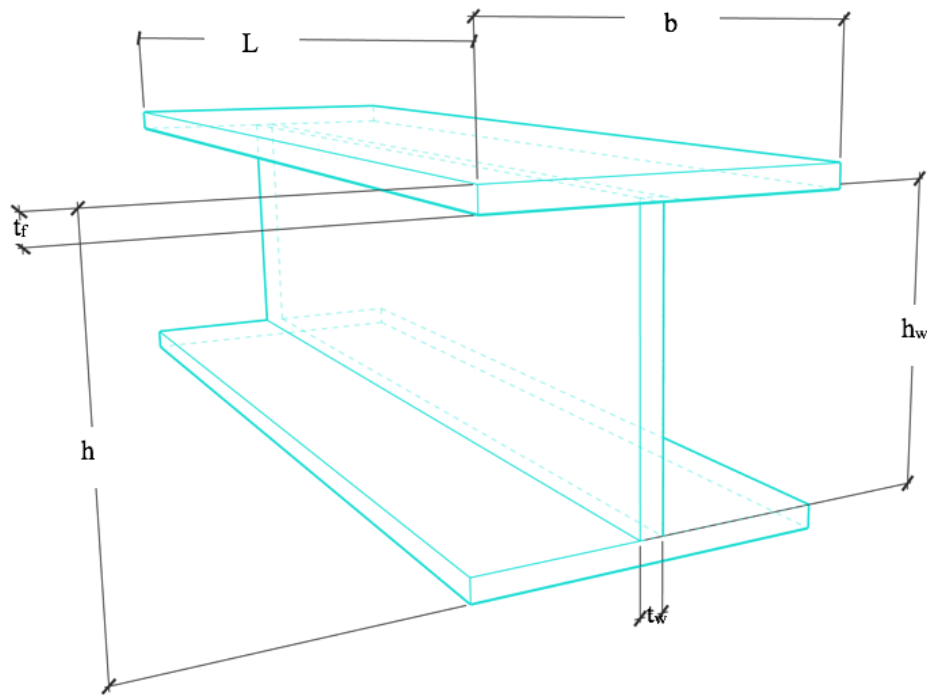


Fig. 2. Nano-sized I-Beam

Previous works shown that the Young's modulus of hybrid or inorganic nano structures can be lower than conventional CNTs which effect directly the stability potential of material [61, 62]. On the other hand, the great advantage of having I-like cross section can pass over the disadvantage of Young's modulus. I-cross section is widely used in civil engineering due to it's high moment of inertia of cross section. The web resists shear forces while the flanges resist most of the bending moment. The I shaped structure have advantages in carrying both bending and shear loads in the plane of the web while having the disadvantage of reduced capacity in the transverse direction, and carrying torsional loads. Also, used material in I-cross section is minimized to needed area. Minimizing the production material is also a great advantage when it comes to work with high-cost nanomaterials.

## 3. Size Dependent Buckling Analysis

In present paper, the size effective stability analysis of simply supported, I-shaped hybrid nanobeam. Deriving the size effective buckling equation based on Eringen's nonlocal elasticity theory [63] is given in detail in literature [60, 64].

$$P(n) = \frac{(\overline{EI} - k_p\mu)\left(\dfrac{n\pi}{L}\right)^4 + (k_w\mu + k_p)\left(\dfrac{n\pi}{L}\right)^2 + k_w}{\mu\left(\dfrac{n\pi}{L}\right)^4 + \left(\dfrac{n\pi}{L}\right)^2} \qquad (1)$$

Herein, *"E"* and *"I"* represent the Young's Modulus and moment of inertia respectively. $\mu$ is the nonlocal parameter. $k_w$ and $k_p$ stand for the Winkler modulus and Pasternak modulus of the elastic foundation which will be neglected in present paper as the nanobeam is modeled without foundation. Young's modulus of hybrid inorganic/organic can vary. Selected Young's modulus for this paper is equal to spinel structured $C_3N_4$ 834 GPa to represent an average hybrid nanobeam [65]. Also, selected size of I-shaped nanobeam is 15nm wide flanges with 2nm thickness while having 20 nm web with 2 nm thickness and 500 nm length. The moment of inertia can be calculated analytically using following formulas;

$$I_{I-shape} = \frac{bh^3 - bh_w^3 + t_w h_w^3}{12} \qquad (2)$$

Nonlocal parameter is;

$$\mu = (1 - e_0 a)^2 \qquad (3)$$
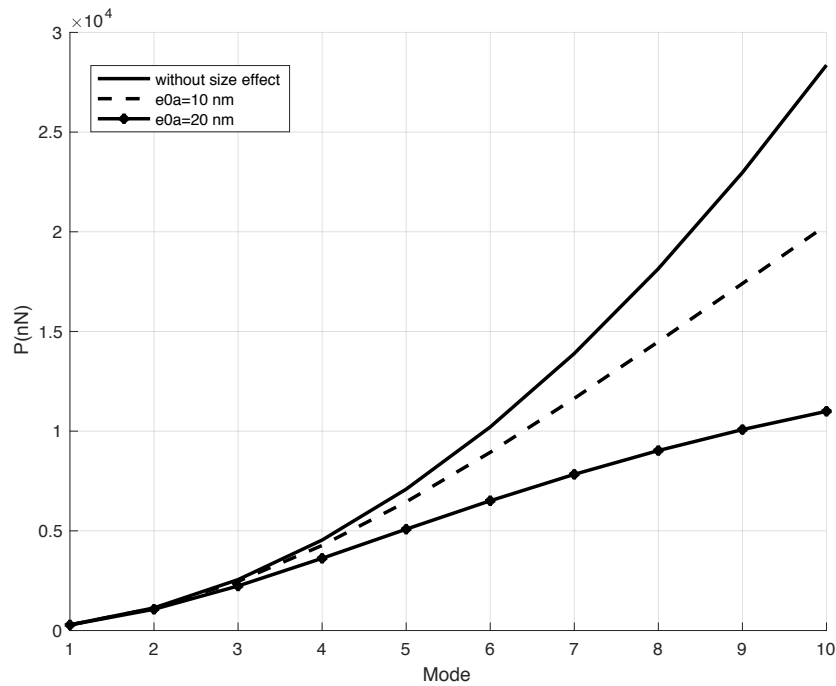


Fig. 3. The variation of buckling load versus mode number

As it can be clearly seen from Fig. 3, the buckling load difference between size effective results and classical theory become dramatic with the rise in mode number. The effect of size dependent theory can be neglected for first modes while it is impossible for higher mode modes. On the other hand, the advantage of high moment of inertia results with higher buckling loads comparing to conventional tubular nanobeams. Together with the rise in moment of inertia the advantage of lower cross-sectional area results with lower production and material cost.

## 4. Conclusions

In this work, the buckling analysis of hybrid organic/inorganic nanobeam with I cross section is investigated by taking the size effect into consideration. Eringen's nonlocal elasticity theory is used. Buckling loads of hybrid inorganic/organic nanobeam for first ten modes is demonstrated in figure using classical theory and Eringen's nonlocal elasticity theory. It is clearly demonstrated that the size effect can be neglected for first modes while it is unneglectable for higher modes. The nanobeam is modeled simply supported without foundation. Further researches can be comparing conventional nanotubes with I cross-sectioned nanobeams using different size effective theory. Comparative results can guide the usage of nanobeams in nano-structures.

## References

[1] Iijima, S., Helical microtubules of graphitic carbon. *Nature*, 354(6348), 56, 1991.

[2] Novoselov, K.S., Geim, A.K., Morozov, S.V., Jiang, D., Zhang, Y., Dubonos, S.V., Grigorieva, I.V., Firsov, A.A., Electric field effect in atomically thin carbon films. *science*, 306(5696), 666-669, 2004.

[3] Mercan, K., Demir, Ç., Akgöz, B., Civalek, O., Coordinate Transformation for Sector and Annular Sector Shaped Graphene Sheets on Silicone Matrix. *International Journal of Engineering & Applied Sciences*, 7(2), 56-73, 2015.

[4] Zhang, J., Ullah, S., Gao, Y., Avcar, M., Civalek, O., Analysis of orthotropic plates by the two-dimensional generalized FIT method. *Computers and Concrete*, 26(5), 421-427, 2020.

[5] Mercan, K., Civalek, O., Modal Analysis of Micro and Nanowires Using Finite Element Softwares. *International Journal of Engineering and Applied Sciences*, 10(4), 291-304, 2018.

[6] Civalek, O., Demir, Ç., Bending analysis of microtubules using nonlocal Euler–Bernoulli beam theory. *Applied Mathematical Modelling*, 35(5), 2053-2067, 2011.

[7] Demir, C., Civalek, O., Torsional and longitudinal frequency and wave response of microtubules based on the nonlocal continuum and nonlocal discrete models. *Applied Mathematical Modelling*, 37(22), 9355-9367, 2013.

[8] Akgöz, B., Civalek, O., Investigation of size effects on static response of single-walled carbon nanotubes based on strain gradient elasticity. *International Journal of Computational Methods*, 9(02), 1240032, 2012.

[9] Jalaei, M.H., Civalek, O., A nonlocal strain gradient refined plate theory for dynamic instability of embedded graphene sheet including thermal effects. *Composite Structures*, 220, 209-220, 2019.

[10] Akgoz, B., Civalek, O., Analysis of microtubules based on strain gradient elasticity and modified couple stress theories. *Advances in Vibration Engineering*, 11(4), 385-400, 2012.

[11] Mercan, K., Emsen, E., Civalek, Ö., Effect of silicon dioxide substrate on buckling behavior of Zinc Oxide nanotubes via size-dependent continuum theories. *Composite Structures*, 218, 130-141, 2019.

[12] Civalek, O., Numanoğlu, H.M., Mercan, K., Finite Element Model and Size Dependent Stability Analysis of Boron Nitride and Silicon Carbide Nanowires/Nanotubes. *Scientia Iranica*, 26(4), 2079-2099, 2019.

[13] Mercan, K., Civalek, O., Buckling analysis of Silicon carbide nanotubes (SiCNTs) with surface effect and nonlocal elasticity using the method of HDQ. *Composites Part B: Engineering*, 114, 34-45, 2017.

[14] Ebrahimi, F., Barati, M.R., Civalek, O., Application of Chebyshev–Ritz method for static stability and vibration analysis of nonlocal microstructure-dependent nanostructures. *Engineering with Computers*, 1-12, 2019.

[15] Akgöz, B., Civalek, O., Vibrational characteristics of embedded microbeams lying on a two-parameter elastic foundation in thermal environment. *Composites Part B: Engineering*, 150, 68-77, 2018.

[16] Numanoglu, H.M., Mercan, K., Civalek, O., Frequency and Mode Shapes of Au Nanowires Using the Continuous Beam Models. *International Journal of Engineering & Applied Sciences*, 9(1), 55-61, 2017.

[17] Mercan, K., Akgöz, B., Demir, Ç., Civalek, O., Frequencies Values of Orthotropic Composite Circular and Annular Plates. *International Journal of Engineering & Applied Sciences*, 9(2), 55-65, 2017.

[18] Demir, Ç., Ersoy, H., Mercan, K., Civalek, O., Free vibration analysis of annular sector plates via conical shell equations. *Curved and Layered Structures*, 4(1), 146-157, 2017.

[19] Demir, Ç., Akgöz, B., Erdinç, M.C., Mercan, K., Civalek, O., Elastik bir ortamdaki grafen tabakanın titreşim hesabı. *Gazi Üniversitesi Mühendislik-Mimarlık Fakültesi Dergisi*, 32(2), 2017.

[20] Emsen, E., Mercan, K., Akgöz, B., Civalek, O., Modal analysis of tapered beam-column embedded in Winkler elastic foundation. *International Journal of Engineering and Applied Sciences*, 7(1), 1-11, 2015.

[21] Civalek, O., Uzun, B., Yaylı, M.Ö., Akgöz, B., Size-dependent transverse and longitudinal vibrations of embedded carbon and silica carbide nanotubes by nonlocal finite element method. *The European Physical Journal Plus*, 135(4), 381, 2020.

[22] Mercan, K., Ersoy, H., Civalek, O., Free Vibration of Annular Plates by Discrete Singular Convolution and Differential Quadrature Methods. *Journal of Applied and Computational Mechanics*, 2(3), 128-133, 2016.

[23] Akgöz, B., Mercan, K., Demir, Ç., Civalek, O., Static analysis of beams on elastic foundation by the method of discrete singular convolution. *International Journal of Engineering and Applied Sciences*, 8(3), 67-73, 2016.

[24] Mercan, K., Demir, Ç., Ersoy, H., Civalek, O., The effects of thickness on frequency values for rotating circular shells. *International Journal of Engineering & Applied Sciences*, 8(1), 26-37, 2016.

[25] Mercan, K., Ebrahimi, F., Civalek, O., Vibration of angle-ply laminated composite circular and annular plates. *Steel and Composite Structures*, 34(1), 141-154, 2020.

[26] Akgöz, B., Civalek, O., A size-dependent beam model for stability of axially loaded carbon nanotubes surrounded by Pasternak elastic foundation. *Composite Structures*, 176, 1028-1038, 2017.

[27] Akgöz, B., Civalek, O., Bending analysis of embedded carbon nanotubes resting on an elastic foundation using strain gradient theory. *Acta Astronautica*, 119, 1-12, 2016.

[28] Demir, C., Mercan, K., Numanoglu, H.M., Civalek, O., Bending response of nanobeams resting on elastic foundation. *Journal of Applied and Computational Mechanics*, 4(2), 105-114, 2018.

[29] Mercan, K., Comparative Stability Analysis of Silicone Carbide Nanotube using MD Simulation and FEM Software. *International Journal of Engineering and Applied Sciences*, 11(4), 507-511, 2019.

[30] Mercan, K., A Comparative Buckling Analysis of Silicon Carbide Nanotube and Boron Nitride Nanotube. *International Journal of Engineering & Applied Sciences*, 8(4), 99-107, 2016.

[31] Mercan, K., Aydoğdu, İ., Civalek, O., Discrete Singular Convolution and Differential Quadrature Method for Buckling Analysis of Laminated Composite Plates. *International Journal of Engineering & Applied Sciences*, 8(4), 66-74, 2016.

[32] Mercan, K., Civalek, O., A Simple Buckling Analysis of Aorta Artery. *International Journal of Engineering & Applied Sciences*, 7(4), 34-44, 2016.

[33] Mercan, K., Civalek, O., DSC method for buckling analysis of boron nitride nanotube (BNNT) surrounded by an elastic matrix. *Composite structures*, 143, 300-309, 2016.

[34] Mercan, K., Civalek, O., Buckling Analysis of Silicon Carbide Nanotubes (SiCNTs). *International Journal of Engineering & Applied Sciences*, 8(2), 101-108, 2016.

[35] Civalek, O., Uzun, B., Yaylı, M.Ö., Stability analysis of nanobeams placed in electromagnetic field using a finite element method. *Arabian Journal of Geosciences*, 13(21), 1165, 2020.

[36] Lv, S., Ma, L., Shen, X., Tong, H., One-step copper-catalyzed synthesis of porous carbon nanotubes for high-performance supercapacitors. *Microporous and Mesoporous Materials*, 310, 110670, 2021.

[37] Akbas, S.D., Mercan, K., Civalek, O., Post-buckling analysis of aorta artery under axial compression loads. *Advances in nano research*, 8(3), 255-264, 2020.

[38] Rodriguez, M.A., Anunziata, O.A., Beltramone, A.R., Martínez, M.L., Multiple-wall carbon nanotubes obtained with mesoporous material decorated with ceria-zirconia. *Materials Letters*, 283, 128900, 2021.

[39] Demir, Ç., Mercan, K., Civalek, O., Determination of critical buckling loads of isotropic, FGM and laminated truncated conical panel. *Composites Part B: Engineering*, 94, 1-10, 2016.

[40] Mercan, K., Demir, Ç., Civalek, O., Vibration analysis of FG cylindrical shells with power-law index using discrete singular convolution technique. *Curved and Layered Structures*, 3(1), 82-90, 2016.

[41] Akgöz, B., Civalek, O., Effects of thermal and shear deformation on vibration response of functionally graded thick composite microbeams. *Composites Part B: Engineering*, 129, 77-87, 2017.

[42] AlSaid-Alwan, H.H.S., Avcar, M., Analytical solution of free vibration of FG beam utilizing different types of beam theories: A comparative study. *Computers and Concrete*, 26(3), 285-292, 2020.

[43] Arefi, M., Firouzeh, S., Mohammad-Rezaei Bidgoli, E., Civalek, O., Analysis of porous micro-plates reinforced with FG-GNPs based on Reddy plate theory. *Composite Structures*, 247, 112391, 2020.

[44] Hadji, L., Avcar, M., Free Vibration Analysis of FG Porous Sandwich Plates under Various Boundary Conditions. *Journal of Applied and Computational Mechanics*, 2020.

[45] Jalaei, M.H., Civalek, O., On dynamic instability of magnetically embedded viscoelastic porous FG nanobeam. *International Journal of Engineering Science*, 143, 14-32, 2019.

[46] Civalek, O., Kiracioglu, O., Free vibration analysis of Timoshenko beams by DSC method. *International Journal for Numerical Methods in Biomedical Engineering*, 26(12), 1890-1898, 2010.

[47] Civalek, O., Yavas, A., Large deflection static analysis of rectangular plates on two parameter elastic foundations. *International Journal of Science and Technology*, 1(1), 43-50, 2006.

[48] Uzun, B., Yaylı, M.Ö., Nonlocal vibration analysis of Ti-6Al-4V/ZrO2 functionally graded nanobeam on elastic matrix. *Arabian Journal of Geosciences*, 13(4), 155, 2020.

[49] Uzun, B., Yaylı, M.Ö., Deliktaş, B., Free vibration of FG nanobeam using a finite-element method. *Micro & Nano Letters*. 15, 35-40, 2020.

[50] Dastjerdi, S., Akgöz, B., Civalek, O., On the effect of viscoelasticity on behavior of gyroscopes. *International Journal of Engineering Science*, 149, 103236, 2020.

[51] Mercan, K., Baltacıoglu, A.K., Civalek, O., Free vibration of laminated and FGM/CNT composites annular thick plates with shear deformation by discrete singular convolution method. *Composite Structures*, 186, 139-153, 2018.

[52] Civalek, O., Avcar, M., Free vibration and buckling analyses of CNT reinforced laminated non-rectangular plates by discrete singular convolution method. *Engineering with Computers*, 2020.

[53] Civalek, O., Geometrically nonlinear dynamic and static analysis of shallow spherical shell resting on two-parameters elastic foundations. *International Journal of Pressure Vessels and Piping*, 113, 1-9, 2014.

[54] Ersoy, H., Mercan, K., Civalek, O., Frequencies of FGM shells and annular plates by the methods of discrete singular convolution and differential quadrature methods. *Composite Structures*, 183, 7-20, 2018.

[55] Civalek, O., Finite Element analysis of plates and shells. Elazığ: Fırat University, 1998.

[56] De Volder, M.F., Tawfick, S.H., Baughman, R.H., Hart, A.J., Carbon nanotubes: present and future commercial applications. *Science*, 339(6119), 535-539, 2013.

[57] Kinloch, I.A., Suhr, J., Lou, J., Young, R.J., Ajayan, P.M., Composites with carbon nanotubes and graphene: An outlook. *Science*, 362(6414), 547-553, 2018.

[58] Elmoselhy, S.A.M., Hybrid Organic/Inorganic Nano-I-Beam for Structural Nano-mechanics. *Scientific Reports*, 9(1), 18324, 2019.

[59] Mercan, K., Civalek, O., Comparison of small scale effect theories for buckling analysis of nanobeams. *International Journal of Engineering and Applied Sciences*, 9(3), 2017.

[60] Mercan, K., Numanoglu, H.M., Akgöz, B., Demir, C., Civalek, O., Higher-order continuum theories for buckling response of silicon carbide nanowires (SiCNWs) on elastic matrix. *Archive of Applied Mechanics*, 87(11), 1797-1814, 2017.

[61] Sim, L.C., Tan, W.H., Leong, K.H., Bashir, M.J., Saravanan, P., Surib, N.A., Mechanistic characteristics of surface modified organic semiconductor g-C3N4 nanotubes alloyed with titania. *Materials*, 10(1), 28, 2017.

[62] Prasad, C., Tang, H., Liu, Q., Bahadur, I., Karlapudi, S., Jiang, Y., A latest overview on photocatalytic application of g-C3N4 based nanostructured materials for hydrogen production. *International Journal of Hydrogen Energy*, 45(1), 337-379, 2020.

[63] Eringen, A.C., Nonlocal continuum field theories, Springer Science & Business Media, 2002.

[64] Civalek, O., Demir, Ç., Akgöz, B., Static analysis of single walled carbon nanotubes (SWCNT) based on Eringen's nonlocal elasticity theory. *International Journal of Engineering and Applied Sciences*, 1(2), 47-56, 2009.

[65] Manyali, G.S., Warmbier, R., Quandt, A., Lowther, J.E., Ab initio study of elastic properties of super hard and graphitic structures of C3N4. *Computational Materials Science*, 69, 299-303, 2013.

**JEAS**

# Buckling Analysis of Intermediately Supported Nanobeams via Strain Gradient Elasticity Theory

*Mustafa Arda*

*Trakya University, Department of Mechanical Engineering, 22130, Edirne, TURKEY*
*E-mail address*: mustafaarda@trakya.edu.tr

*ORCID number of author:*
*0000-0002-0314-3950*

**Abstract**

*Buckling of axially loaded cantilever nanobeams with intermediate support have been studied in the current study. Higher order size dependent strain gradient theory has been utilized to capture the scale effect in nano dimension. Minimum total potential energy formulation has been used in modeling of nanobeam. Approximate Ritz method has been applied to the energy formulation for obtaining critical buckling loads. Position of the intermediate support has been varied and its effect on the critical buckling load has been investigated in the analysis. Mode shapes in critical buckling loads have been shown for various intermediate support positions. Present results could be useful in design of carbon nanotube resonators.*

**Keywords:** Nanobeam, Strain Gradient, Intermediate Support, Ritz Method.

## 1. Introduction

Carbon nanotubes (CNTs) have had an increasing popularity over the last three decades in academia and industry. Superior properties like thermal, electromagnetic, strength, etc. have enriched the possible usage areas of CNTs [1–3].

Statics and dynamics of nanoscale structures can be achieved with higher order size dependent continuum mechanics theories: strain gradient [4], stress gradient [5,6], couple stress[7], doublet mechanics[8] and peridynamics [9]. It has been presented in earlier works that classical elasticity theory is inadequate in the modelling of CNTs due to its size independent characteristics.

Basis of the higher order size dependent theories went back to a century ago. Cauchy [10], Voigt [11] and Cosserat brothers [12] had constituted the higher gradient elasticity theory. Kunin [13] , Toupin [14], Mindlin [15], Kröner [16], Green and Rivlin [17] improved the higher order elasticity theories with including microstructural effects.

Eringen [18] proposed the nonlocal elasticity theory which is a stress gradient model. After Eringen, Aifantis and coworkers [19–22], proposed a higher order strain gradient elasticity theory for finite and infinitesimal deformations. Theories of Eringen and Aifantis are comparatively simple and includes less number of higher order gradient terms than previous

ones. Higher order strain gradient models have been applied to the buckling problem of nano structures in several papers [23–32] . Over the last 20 years, higher order stress and strain driven continuum mechanics theories have been used in many studies [33–46].

In the present study, strain gradient nanobeam model has been developed for the buckling of axially loaded cantilever nanobeam with intermediate support. Higher order governing equation of motion for nanobeam have been obtained with minimum total potential energy formulation. Approximate Ritz Method has been used in the solution of the governing equation of motion. Effect of the position of intermediate support to the critical buckling load of nanobeam. Mode shapes at critical buckling loads for the first three modes have been depicted in various position of intermediate support. Differently from the previous studies, position of the intermediate support has been investigated in buckling case using strain gradient theory.

## 2. Analysis

A nanobeam of hollow tube with length $L$ is considered (Fig. 1). $x$ and $z$ axes define the axial length direction and transverse direction of nanobeam, respectively. $P$ is the external axial load and position of the intermediate support is defined as $\eta L$.
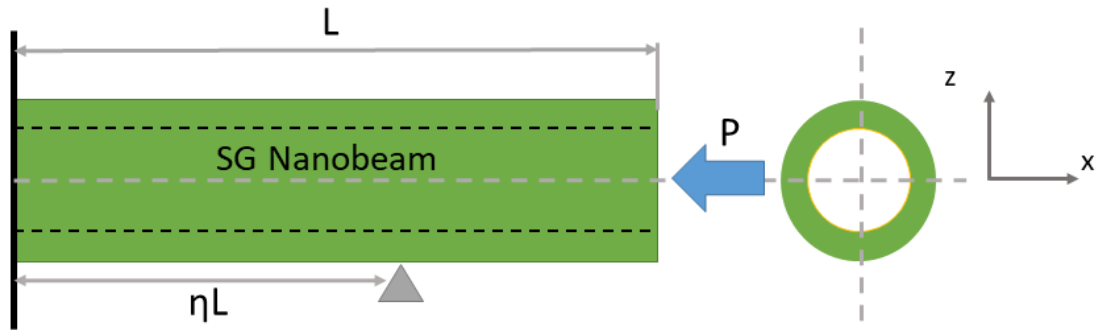


Fig. 1. Axially Loaded Nanobeam with Intermediate Support

### 2.1. Strain Gradient Theory

Refined form of the strain gradient elasticity theory can be interpreted for stress-strain relation as below [19–22]:

$$\sigma_{ij} = \lambda \bar{\varepsilon}_{kk} \delta_{ij} + 2\mu \bar{\varepsilon}_{ij} \quad , \quad \bar{\varepsilon}_{ij} = \varepsilon_{ij} - l\nabla^2 \varepsilon_{ij} \tag{1}$$

where $\sigma$ and $\varepsilon$ are the stress and strain tensors for elastic deformation respectively, $\nabla$ is the Laplacian, $\lambda$ and $\mu$ are the standard Lame constants and $l$ is the strain gradient parameter.

If the constituve equation is reformulated for one dimensional structures, the stress strain relation for the nanobeam can be obtained:

$$\sigma_{xx} = \left(1 - l\frac{\partial^2}{\partial x^2}\right) E\varepsilon_{xx} \tag{2}$$

Total potential energies for the nanobeam can be defined as below:

$$T = \frac{1}{2}\int_0^L P\left(\frac{\partial w}{\partial x}\right)^2 dx \tag{3}$$

$$U = \frac{1}{2}\int_0^L EI \left(\frac{\partial^2 w}{\partial x^2}\right)^2 dx + \frac{1}{2}\int_0^L lEI \left(\frac{\partial^3 w}{\partial x^3}\right)^2 dx \tag{4}$$

where $I$ is moment of inertia for the nanobeam, $T$ defines the work done by external axial load and $U$ defines the potential energy of nanobeam. It should be noted that there is no kinetic energy in the present static buckling problem.

## 2.2. Ritz method

Analytical solution of the higher order governing equation of motions becomes complicated and time consuming with increasing number of boundary conditions and integration constants. Ritz method is a useful approximate variational method can be used in the solution of the mentioned problem [47–49]. Also discrete singular convolution method [50–53] and finite element modelling [54] can be used as an approximate solution.

Displacement function can be defined as in the below form for the Ritz method [55]:

$$w(\bar{x}) = \sum_{j=j_0}^{J} A_j \psi_j(\bar{x}) \tag{5}$$

where $\bar{x}$ is the dimensionless nanobeam length $\left(\bar{x} = \frac{x}{L}\right)$, $A_j$'s are the unknown coefficients and $\psi_j(\bar{x})$ is a function which satisfies geometric boundary conditions of the beam. Convergence of this function is satisfied if this function is mathematically complete set. To determine the critical buckling of nanobeam, next functional is defined:

$$F = T_{max} - U_{max} \tag{6}$$

This functional should be minimized with respect to unknown coefficients given in Eq. (5):

$$\frac{\partial F}{\partial A_{\bar{j}}} = 0 \quad , \quad \bar{j} = \bar{j}_0, \dots, J \tag{7}$$

$$F = \frac{1}{2}\int_0^1 P_{cr} \frac{\partial w}{\partial \bar{x}} \frac{\partial \bar{w}}{\partial \bar{x}} d\bar{x} - \frac{1}{2}\int_0^1 \frac{\partial^2 w}{\partial \bar{x}^2} \frac{\partial^2 \bar{w}}{\partial \bar{x}^2} d\bar{x} - \frac{1}{2}\int_0^1 \frac{l}{L^2} \frac{\partial^3 w}{\partial \bar{x}^3} \frac{\partial^3 \bar{w}}{\partial \bar{x}^3} d\bar{x} \tag{8}$$

where $P_{cr}$ is the dimensionless critical buckling load of nanobeam and defined as below:

$$P_{cr} = \frac{PL^2}{EI} \tag{9}$$

Eq. (8) gives a total of $J \times J$ simultaneous, linear, homogeneous equations in an equal number of unknowns $A_j$. Those equations can be described as an eigen-value problem for critical buckling load. The mode shapes corresponding to any $P_{cr}$ is found by substituting that value into Eq. (7) and solving for the eigenvector components $A_j/A_1$. Inserting these components into Eq. (7) gives mode shape of nanobeam.

$\psi_j(\bar{x})$ polynomial can be assumed as below in general form.

$$\psi_j = (\bar{x} - 0)^{b_1}(\bar{x} - \eta)^{b_2}(\bar{x} - 1)^{b_3}(\bar{x}^{j-1}) \tag{10}$$

where $b_1$, $b_2$ and $b_3$ parameters define the boundary conditions and should be selected as 0, 1, 2 for the free, simply supported and clamped boundary conditions, respectively. For the present clamped-simply supported-free nanobeam case, Eq. (10) turns into:

$$\psi_j = (\bar{x})^2 (\bar{x} - \eta)(\bar{x}^{j-1}) \tag{11}$$

## 3. Numerical Results

Buckling analysis of the axially loaded nanobeam has been carried out for position of intermediate support and strain gradient parameter in this section. Analysis has been made independent from the material properties, except the nanobeam length which is assumed 5nm. Interested readers can look to previous paper [56] about selection of the length scale parameter.

Convergence of the Ritz method is seen in Table 1 for the first three critical buckling loads on local($l$=0) clamped-free and clamped-simply supported beams. Ritz method converges to literature works when $J$ is assumed as 7.

Table 1. Validation of the Ritz Solution

| Mode Number | Clamped-Free | | Clamped-Simply Supported | |
|---|---|---|---|---|
| | $P_{cr} = \dfrac{\pi^2}{4}$ | Ritz Method | $P_{cr} = \dfrac{\pi^2}{0.7^2}$ | Ritz Method |
| 1 | 2.4674 | 2.4674 | 20.1907 | 20.1907 |
| 2 | 22.2066 | 22.2066 | 59.6795 | 59.6803 |
| 3 | 61.6850 | 61.7017 | 118.9000 | 119.0870 |

In Table 2, strain gradient parameter effect on critical buckling load can be seen. Strain gradient theory exhibits stiffening effect on structure. Growing rigidity increases the critical buckling load. Position of the intermediate support should be investigated with using both Table 2 and Figure 2. Critical buckling load increases when intermediate support approaches to the free end at the first mode. On the other hand, second and third mode critical buckling loads firstly increase, then goes constant little bit and decreases after that. Third mode buckling load also initially increases than start to decrease. Cause of this behavior should be related with the nodal points of mode shapes which can be seen in Figures 3 and 4. If the intermediate support is placed after a nodal point, nanobeam can buckle more easily.

Table 2. Strain Gradient Theory Effect on Critical Buckling Loads

| Mode Number | Local Theory ($l$=0) | | | Strain Gradient Theory ($l$=0.1nm$^2$) | | |
|---|---|---|---|---|---|---|
| | $\eta$=0.1 | $\eta$=0.5 | $\eta$=1 | $\eta$=0.1 | $\eta$=0.5 | $\eta$=1 |
| 1 | 2.8912 | 6.2714 | 20.1907 | 3.2152 | 6.6923 | 21.7518 |
| 2 | 26.0184 | 52.2509 | 59.6803 | 31.0665 | 62.4753 | 72.4724 |
| 3 | 72.2408 | 120.7560 | 119.0870 | 97.9405 | 171.5440 | 169.417 |
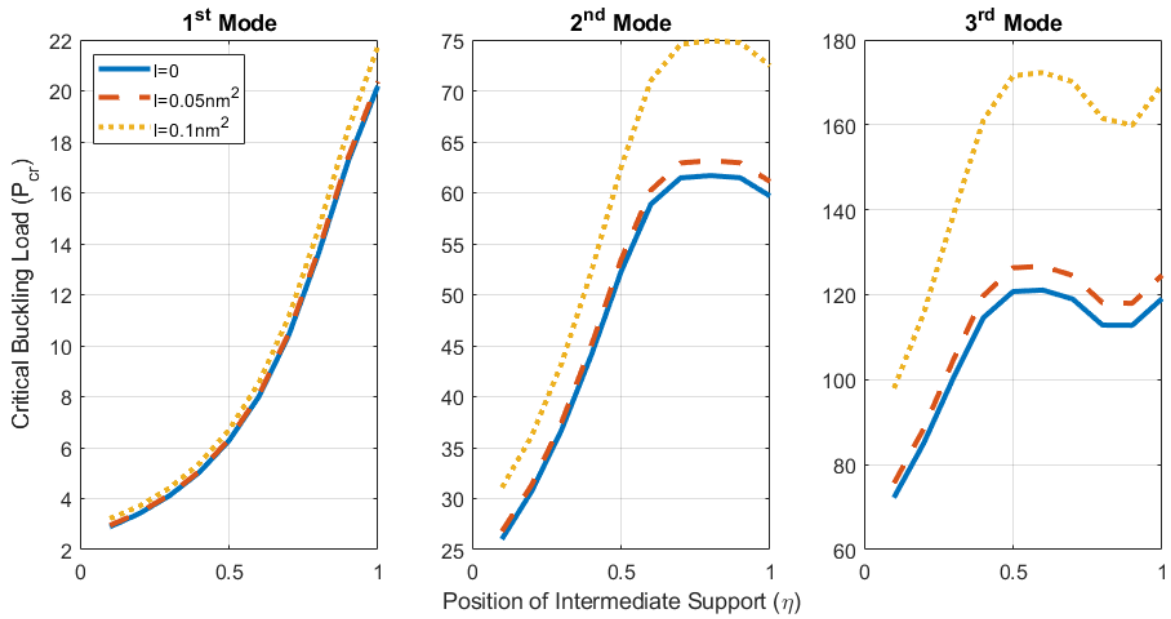
Fig. 2. Variation of Critical Buckling Load with Position of Intermediate Support

In Figures 3 and 4, mode shapes of nanobeam at the first three critical buckling loads are seen. Increasing critical buckling load enhances the relative amplitude of displacements. Position of the intermediate support has an important effect on mode shapes. Also, strain gradient theory increases the amplitudes in mode shapes as a result of increasing critical buckling load.
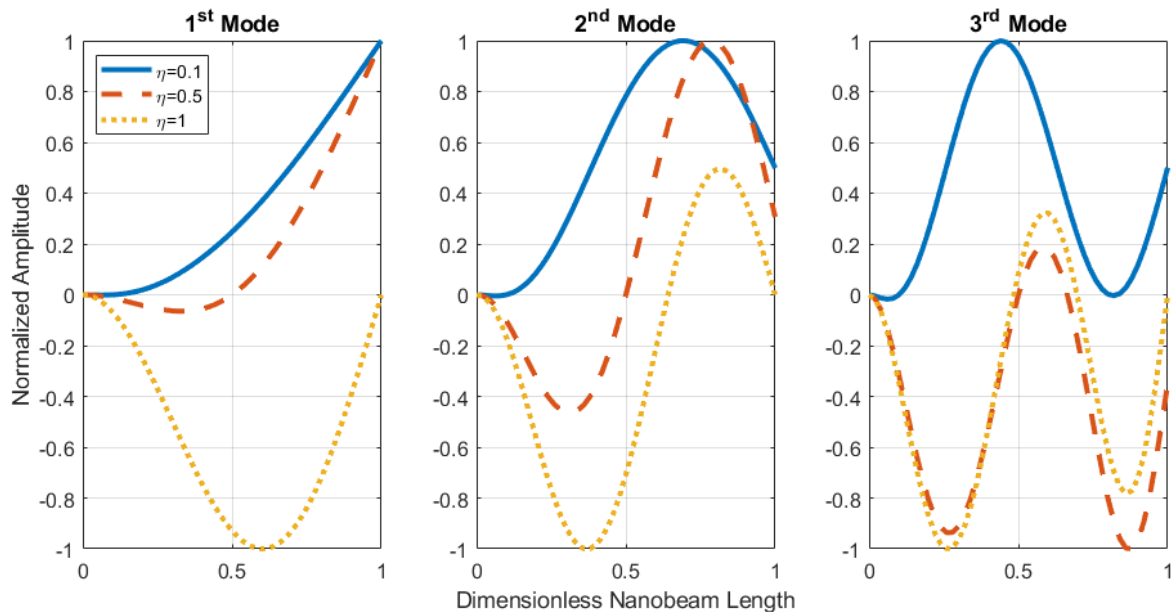


Fig. 3. Mode Shapes of Nanobeam at Various Intermediate Support Positions (*l*=0)
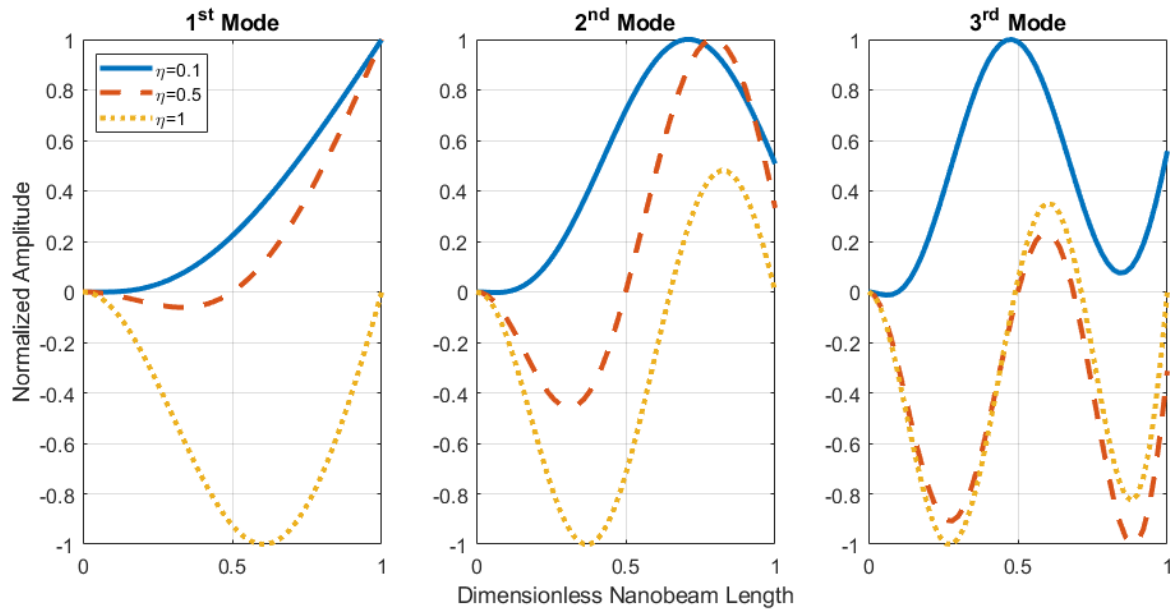
Fig. 4. Mode Shapes of Nanobeam at Various Intermediate Support Positions ($l$=0.1nm$^2$)

## 4. Conclusion

Present study has been investigated the buckling of axially loaded clamped-simply supported-free nanobeams with using strain gradient theory. Minimum total potential energy formulation has been applied to the nanobeam to obtain the static equilibrium equation. Ritz method has been used on the energy formulation for obtaining of critical buckling load. Effects of the position of the intermediate support and strain gradient parameter to the critical buckling load has been investigated. Mode shapes in critical buckling loads have been depicted for local and strain gradient models in various intermediate support positions.

Strain gradient model increases the critical buckling load for nanobeam and normalized amplitudes with the stiffening effect. Position of the intermediate support increase or decrease the critical buckling load depending on the nodal points of adjacent mode numbers.

Present results could be useful in design of carbon nanotube resonators.

## References

[1] Ajiki H., Ando T., Energy Bands of Carbon Nanotubes in Magnetic Fields, *Journal of the Physical Society of Japan*, 65, 505–14, 1996. doi:10.1143/JPSJ.65.505

[2] Craighead H.G., Nanoelectromechanical Systems, *Science*, 290, 1532–5, 2000. doi:10.1126/science.290.5496.1532

[3] Huang X.M.H., Zorman C.A., Mehregany M., Roukes M.L., Nanoelectromechanical systems: Nanodevice motion at microwave frequencies, *Nature*, 421, 496–496, 2003. doi:10.1038/421496a

[4] Ghorbanpour Arani A., Shokravi M., Vibration response of visco-elastically coupled double-layered visco-elastic graphene sheet systems subjected to magnetic field via strain

gradient theory considering surface stress effects, *Proceedings of the Institution of Mechanical Engineers, Part N: Journal of Nanoengineering and Nanosystems*, 229, 180–90, 2015. doi:10.1177/1740349914529102

[5] Arda M., Aydogdu M., Torsional statics and dynamics of nanotubes embedded in an elastic medium, *Composite Structures*, 114, 80–91, 2014. doi:10.1016/j.compstruct.2014.03.053

[6] Li C., Li S., Zhu Z., Prediction of mechanical properties of microstructures through a nonlocal stress field theory, *Proceedings of the Institution of Mechanical Engineers, Part N: Journal of Nanoengineering and Nanosystems*, 229, 50–4, 2015. doi:10.1177/1740349913519437

[7] Kumar M., Reddy G.J., Kumar N.N., Bég O.A., Computational study of unsteady couple stress magnetic nanofluid flow from a stretching sheet with Ohmic dissipation, *Proceedings of the Institution of Mechanical Engineers, Part N: Journal of Nanomaterials, Nanoengineering and Nanosystems*, 233, 49–63, 2019. doi:10.1177/2397791419843730

[8] Gul U., Aydogdu M., Gaygusuzoglu G., Axial dynamics of a nanorod embedded in an elastic medium using doublet mechanics, *Composite Structures*, 160, 1268–78, 2017. doi:10.1016/j.compstruct.2016.11.023

[9] Oterkus E., Diyaroglu C., Zhu N., Oterkus S., Madenci E., Utilization of Peridynamic Theory for Modeling at the Nano-Scale, 2015, p. 1–16. doi:10.1007/978-3-319-21194-7_1

[10] Cauchy A.-L., Mémoire sur les systèmes isotropes de points matériels. Oeuvres complètes, Cambridge University Press, 1882. doi:10.1017/CBO9780511702280.023

[11] Voigt W., Theoretische Studien über die Elasticitätsverhältnisse der Krystalle, *Abhandlungen der Königlichen Gesellschaft der Wissenschaften in Göttingen*, 34, 3–52, 1887

[12] Cosserat E., Cosserat F., Theorie des corps dédormables. A. Hermann et fils, 1909

[13] Kunin I.A., Elastic Media with Microstructure I. vol. 26. Springer Berlin Heidelberg, 1982. doi:10.1007/978-3-642-81748-9

[14] Toupin R.A., Theories of elasticity with couple-stress, *Archive for Rational Mechanics and Analysis*, 17, 85–112, 1964. doi:10.1007/BF00253050

[15] Mindlin R.D., Micro-structure in linear elasticity, *Archive for Rational Mechanics and Analysis*, 16, 51–78, 1964. doi:10.1007/BF00248490

[16] Kröner E., Elasticity theory of materials with long range cohesive forces, *International Journal of Solids and Structures*, 3, 731–42, 1967. doi:10.1016/0020-7683(67)90049-2

[17] Green A.E., Rivlin R.S., Multipolar continuum mechanics, *Archive for Rational Mechanics and Analysis*, 17, 113–47, 1964. doi:10.1007/BF00253051

[18] Eringen A.C., Edelen D.G.B., On nonlocal elasticity, *International Journal of Engineering Science*, 10, 233–48, 1972. doi:10.1016/0020-7225(72)90039-0

[19] Ru C.Q., Aifantis E.C., A simple approach to solve boundary-value problems in gradient elasticity, *Acta Mechanica*, 101, 59–68, 1993. doi:10.1007/BF01175597

[20] Altan B.S., Aifantis E.C., On Some Aspects in the Special Theory of Gradient Elasticity, *Journal of the Mechanical Behavior of Materials*, 8, 1997. doi:10.1515/JMBM.1997.8.3.231

[21] Aifantis E.C., Strain gradient interpretation of size effects, *International Journal of Fracture*, 95, 299–314, 1999

[22] Aifantis E.C., Higher Order Gradients and Self-Organization at Nano, Micro, and Macro Scales, *Materials Science Forum*, 123–125, 553–66, 1993. doi:10.4028/www.scientific.net/msf.123-125.553

[23] Akgöz B., Civalek Ö., Strain gradient elasticity and modified couple stress models for buckling analysis of axially loaded micro-scaled beams, *International Journal of Engineering Science*, 49, 1268–80, 2011. doi:10.1016/j.ijengsci.2010.12.009

[24] Akgöz B., Civalek Ö., Buckling analysis of functionally graded microbeams based on the strain gradient theory, *Acta Mechanica*, 224, 2185–201, 2013. doi:10.1007/s00707-013-0883-5

[25] Akgöz B., Civalek Ö., A new trigonometric beam model for buckling of strain gradient microbeams, *International Journal of Mechanical Sciences*, 81, 88–94, 2014. doi:10.1016/j.ijmecsci.2014.02.013

[26] Mercan K., Civalek Ö., A Simple Buckling Analysis Of Aorta Artery, *International Journal Of Engineering & Applied Sciences*, 7, 34–34, 2015. doi:10.24107/ijeas.251256

[27] Demir Ç., Mercan K., Civalek O., Determination of critical buckling loads of isotropic, FGM and laminated truncated conical panel, *Composites Part B: Engineering*, 94, 1–10, 2016. doi:10.1016/j.compositesb.2016.03.031

[28] Mercan K., Civalek Ö., Buckling Analysis of Silicon Carbide Nanotubes (SiCNTs), *International Journal Of Engineering & Applied Sciences*, 8, 101–101, 2016. doi:10.24107/ijeas.252148

[29] Arda M., Aydogdu M., Buckling of Eccentrically Loaded Carbon Nanotubes, *Solid State Phenomena*, 267, 151–6, 2017. doi:10.4028/www.scientific.net/SSP.267.151

[30] Mercan K., Civalek Ö., Buckling analysis of Silicon carbide nanotubes (SiCNTs) with surface effect and nonlocal elasticity using the method of HDQ, *Composites Part B: Engineering*, 114, 34–45, 2017. doi:10.1016/j.compositesb.2017.01.067

[31] Mercan K., Civalek Ö., Comparison of small scale effect theories for buckling analysis of nanobeams, *International Journal Of Engineering & Applied Sciences*, 9, 87–97, 2017. doi:10.24107/ijeas.340958

[32] Mercan K., Numanoglu H.M., Akgöz B., Demir C., Civalek., Higher-order continuum theories for buckling response of silicon carbide nanowires (SiCNWs) on elastic matrix, *Archive of Applied Mechanics*, 87, 1797–814, 2017. doi:10.1007/s00419-017-1288-z

[33] Civalek Ö., Geometrically nonlinear dynamic and static analysis of shallow spherical shell resting on two-parameters elastic foundations, *International Journal of Pressure Vessels and Piping*, 113, 1–9, 2014. doi:10.1016/j.ijpvp.2013.10.014

[34] Arda M., Aydogdu M., Analysis of Free Torsional Vibration in Carbon Nanotubes Embedded in a Viscoelastic Medium, *Advances in Science and Technology Research Journal*, 9, 28–33, 2015. doi:10.12913/22998624/2361

[35] Ebrahimi F., Barati M.R., Civalek Ö., Application of Chebyshev–Ritz method for static stability and vibration analysis of nonlocal microstructure-dependent nanostructures, *Engineering with Computers*, 36, 953–64, 2020. doi:10.1007/s00366-019-00742-z

[36] AlSaid-Alwan H.H.S., Avcar M., AlSaid-Alwan H.H.S., Avcar M., Analytical solution of free vibration of FG beam utilizing different types of beam theories: A comparative study, *Computers and Concrete*, 26, 285, 2020. doi:10.12989/CAC.2020.26.3.285

[37] Zhang J.S.Y.M.O., Analysis of orthotropic plates by the two-dimensional generalized FIT method, *Computers and Concrete*, 26, 421–7, 2020. doi:10.12989/CAC.2020.26.5.421

[38] Hadji L., Avcar M., Free Vibration Analysis of FG Porous Sandwich Plates under Various Boundary Conditions, *J Appl Comput Mech*, 0, 1–15, 2020. doi:10.22055/JACM.2020.35328.2628

[39] Arda M., Aydogdu M., Bending of CNTs Under The Partial Uniform Load, *International Journal Of Engineering & Applied Sciences*, 8, 21–21, 2016. doi:10.24107/ijeas.252142

[40] Arda M., Aydogdu M., Longitudinal Vibration of CNTs Viscously Damped in Span, *International Journal Of Engineering & Applied Sciences*, 9, 22–22, 2017. doi:10.24107/ijeas.305348

[41] Mercan K., Civalek Ö., What is The Correct Mechanical Model of Aorta Artery, *International Journal Of Engineering & Applied Sciences*, 9, 138–138, 2017. doi:10.24107/ijeas.322526

[42] Akgöz B., Civalek Ö., A size-dependent beam model for stability of axially loaded carbon nanotubes surrounded by Pasternak elastic foundation, *Composite Structures*, 176, 1028–38, 2017. doi:10.1016/j.compstruct.2017.06.039

[43] Arda M., Vibration Analysis of an Axially Loaded Viscoelastic Nanobeam, *International Journal Of Engineering & Applied Sciences*, 10, 252–63, 2018. doi:10.24107/ijeas.468769

[44] Arda M., Aydogdu M., Dynamic stability of harmonically excited nanobeams including axial inertia, *JVC/Journal of Vibration and Control*, 25, 820–33, 2019. doi:10.1177/1077546318802430

[45] Arda M., Aydogdu M., Torsional dynamics of coaxial nanotubes with different lengths in viscoelastic medium, *Microsystem Technologies*, 25, 3943–57, 2019. doi:10.1007/s00542-019-04446-8

[46] Jalaei M.H., Civalek., On dynamic instability of magnetically embedded viscoelastic porous FG nanobeam, *International Journal of Engineering Science*, 143, 14–32, 2019. doi:10.1016/j.ijengsci.2019.06.013

[47] Aydogdu M., Arda M., Filiz S., Vibration of axially functionally graded nano rods and beams with a variable nonlocal parameter, *Advances in Nano Research*, 6, 257–78, 2018. doi:10.12989/anr.2018.6.3.257

[48] Arda M., Aydogdu M., Vibration analysis of carbon nanotube mass sensors considering both inertia and stiffness of the detected mass, *Mechanics Based Design of Structures and Machines*, 0, 1–17, 2020. doi:10.1080/15397734.2020.1728548

[49] Arda M., Axial dynamics of functionally graded Rayleigh-Bishop nanorods, *Microsystem Technologies*, 2, 2020. doi:10.1007/s00542-020-04950-2

[50] Civalek O., Yavas A., Large Deflection Static Analysis of Rectangular Plates On Two Parameter Elastic Foundations, *International Journal of Science and Technology*, 1, 43–50, 2006

[51] Civalek Ö., Kiracioglu O., Free vibration analysis of Timoshenko beams by DSC method,

*International Journal for Numerical Methods in Biomedical Engineering*, 26, 1890–8, 2010. doi:10.1002/cnm.1279

[52] Mercan K., Demir Ç., Civalek Ö., Vibration analysis of FG cylindrical shells with power-law index using discrete singular convolution technique, *Curved and Layered Structures*, 3, 82–90, 2016. doi:10.1515/cls-2016-0007

[53] Civalek Ö., Avcar M., Free vibration and buckling analyses of CNT reinforced laminated non-rectangular plates by discrete singular convolution method, *Engineering with Computers*, 1–33, 2020. doi:10.1007/s00366-020-01168-8

[54] Civalek Ö., Uzun B., Yaylı M.Ö., Akgöz B., Size-dependent transverse and longitudinal vibrations of embedded carbon and silica carbide nanotubes by nonlocal finite element method, *European Physical Journal Plus*, 135, 381, 2020. doi:10.1140/epjp/s13360-020-00385-w

[55] Wright E.M., Kantorovich L. V., Krylov V.I., Benster C.D., Approximate Methods of Higher Analysis, *The Mathematical Gazette*, 44, 145, 1960. doi:10.2307/3612589

[56] Arda M., Evaluation of optimum length scale parameters in longitudinal wave propagation on nonlocal strain gradient carbon nanotubes by lattice dynamics, *Mechanics Based Design of Structures and Machines*, 1–24, 2020. doi:10.1080/15397734.2020.1835488